Collapse of microbubbles over an elastoplastic wall

Dario Abbondanza[1], Mirko Gallo[1] and Carlo Massimo Casciola[1],†

[1]Dipartimento di Ingegneria Meccanica e Aerospaziale, Sapienza Università di Roma, Via Eudossiana 18, 00184 Roma, Italy

The collapse of a vapour bubble over a material surface has been widely studied over the past few decades, but a comprehensive and quantitative analysis of the cavitation dynamics and its effects on solid materials at the mesoscale (nanometre up to micrometre), which would be of particular interest in applications exploiting cavitation power, is still lacking. In this work, we adopt a diffuse interface model to describe the microbubble dynamics, and a dynamic plasticity model for the solid. The former is particularly suited to studying the rich phenomenology characterising bubble collapse at the mesoscale, which comprises transitions to supercritical conditions, emission and propagation of shock waves, generation of liquid microjets and topological transitions, whereas the latter is used to characterise the permanent plastic deformation caused by the bubble collapse, and has been augmented to consider inertial effects, to assess whether or not an interaction between elastic and plastic waves may influence the resulting deformation. Results concerning the collapse of a microbubble at different liquid overpressures and initial standoff ratios are discussed, and the elastoplastic wave propagation in the solid, together with plastic deformation, is studied for different cases, depending on elastic and plastic material parameters.

Key words: bubble dynamics, cavitation

1. Introduction

Bubble collapse near solid boundaries involves high speeds, high energy densities and very small time and length scales. This intense and fast energy release is the origin of the destructive potential of bubble cavitation, well known to be detrimental to the material surface. In fact, apart from the negative effect on hydraulic turbines and other applications

† Email address for correspondence: carlomassimo.casciola@uniroma1.it

in power engineering (Stripling & Acosta 1962), cavitation can be exploited in many contexts, such as industrial cleaning processes (Brems *et al.* 2013), nanomaterials synthesis (Xu, Zeiger & Suslick 2013), kidney stones fragmentation in shock wave lithotripsy, (Zhong 2013), root canal treatment in dentistry (Robinson *et al.* 2018), ophthalmic surgery (Vogel *et al.* 1986) and drug permeability enhancement of overall tissues or cell membranes (Coussios & Roy 2008; Brennen 2015; Peruzzi *et al.* 2018; Silvani *et al.* 2019). The implosion of small bubbles is relevant also for botany, for example in the spore dispersal of ferns (Noblin *et al.* 2012; Scognamiglio *et al.* 2018) or for the embolism of plant xylems under drought (Vincent *et al.* 2012; Ponomarenko *et al.* 2014). In most of these applications, the bubbles are relatively small, typically micrometre size. Despite their size, which may lead one to think that inertial effects are negligible, the damaging potential of micrometre-sized bubbles is, in fact, unexpectedly large.

From the experimental side, much work accumulated starting from the pioneering experiments carried out in Lauterborn's group using millimetre-sized laser-induced bubbles (Lauterborn & Bolle 1975) that inspired much successive work (Occhicone *et al.* 2019; Sinibaldi *et al.* 2019; Bokman *et al.* 2023). High-speed visualisations showed complex dynamics where the imploding bubble loses its spherical symmetry, due to the wall that inhibits the motion of the proximal part of the bubble, at the same time increasing the speed of the distal part. As a consequence, a strong water jet pierces the bubble, changing its topology from a spheroid into a toroid, while at the same time a complex system of compression waves is launched into the liquid. The combined action of the jet and the shock wave violently stresses the wall material inducing its damage in the form of pitting.

Different surfaces have been investigated in the past, including rigid walls (Tomita & Shima 1986; Zhang, Duncan & Chahine 1993; Brujan *et al.* 2002; Johnsen & Colonius 2009; Gonzalez-Avila, Denner & Ohl 2021; Saini *et al.* 2022), elastic solids (Brujan *et al.* 2001), soft tissues (Kodama & Takayama 1998), porous plates (Andrews, Rivas & Peters 2023) and free liquid–gas interfaces (Robinson *et al.* 2001). Plastic deformation has also been addressed in a number of papers, see e.g. Philipp & Lauterborn (1998), Dular, Delgosha & Petkovšek (2013) and Dular *et al.* (2019), where the shape and size of the indentations were measured accurately.

Concerning numerical simulations, several works that coupled the dynamics of the fluid–solid system emerged in recent years (Chahine & Hsiao 2015; Cao *et al.* 2021). In most of these cases, the focus was on relatively large, macroscopic bubbles, where the relevant physics is essentially described by the inviscid Euler equation for the only liquid phase (Johnsen & Colonius 2009; Rasthofer *et al.* 2019).

With the advent of microtechnologies, experiments are now pushed to the submillimetre range (Ohl & Ikink 2003; Tho, Manasseh & Ooi 2007; Wu *et al.* 2021; Pfeiffer *et al.* 2022; Gutiérrez-Hernández *et al.* 2023). Significant effort is currently aimed at understanding how the material surface is affected by the collapsing bubble, particularly concerning clinical and biophysical applications (Miller, Pislaru & Greenleaf 2002; Adhikari, Goliaei & Berkowitz 2016; Mancia *et al.* 2019; Barney *et al.* 2020), and industrial cleaning processes (Zeng *et al.* 2018; Zeng, An & Ohl 2022; Reese, Ohl & Ohl 2023; Mnich *et al.* 2024). It is the purpose of the present paper to discuss the response of the material surface to the implosion of such small vapour bubbles, where surface tension, viscosity and phase change are intermingled, calling for a comprehensive model encompassing all the phenomenologies occurring along bubble collapse (Magaletti, Marino & Casciola 2015; Magaletti *et al.* 2016). The bubble is assumed to be already present in the liquid, with no regard to the nucleation process that led to the bubble formation, see Gallo, Magaletti &

Casciola (2018, 2021), Gallo *et al.* (2020, 2023) and Magaletti, Gallo & Casciola (2021) for details on nucleation in the context of this kind of model. The wall is assumed flat and the analysis will concern the deformation of the solid, assumed as an elastoplastic material. Given the small size of the bubble, and the need to simultaneously account for the liquid compressibility, the dynamic response of the bubble gaseous phase, the phase change taking place in the vapour and the topology modification occurring during the collapse, the model of choice is a phase-field method (Anderson, McFadden & Wheeler 1998; Jamet 2001; Magaletti *et al.* 2013; Hu, Wang & Gomez 2023) described in terms of mass density and accounting for surface tension through distributed capillary stresses, as originally introduced by van der Waals (1893, 1979). The solid is basically described by the linear elasticity equations (Gurtin 1982) on account of the expected small deformation of the solid. Indeed, the scope of the present paper is limited to relatively stiff materials which are hardly deformed, leaving for future investigations the case of softer materials, such as hydrogels (Guvendiren & Burdick 2012; Liu, Toh & Ng 2015; Drozdov & de Claville Christiansen 2018) or tissues and cell membranes (Bottacchiari *et al.* 2022). As we show, despite the relatively large stiffness leading to small deformations, the state of tension undergone by the solid under the pressure field of the collapsing bubble is rather large and may easily exceed the yield stress of many materials (Abbondanza, Gallo & Casciola 2023*a*).

At variance with most applications of elastoplastic materials in structural engineering, the load exerted on the solid is highly non-stationary, inducing a complex response where elastic wave propagation is combined with unsteady plastic deformation (Von Kármán & Duwez 1950). Moreover, due to the presence of the fluid–solid interface subject to the bubble pressure load propagating at a fast speed, the system of elastic waves turns out to be rather rich. As is well known, linear elastic solids support the propagation of two substantially different kinds of (bulk) waves: longitudinal, or compression, waves, travelling at the speed $c_L = \sqrt{(K + 4/3G)/\rho_s}$, where K and G are the bulk and the shear moduli, respectively, with ρ_s the solid mass density; and transversal, or shear, waves with speed $c_T = \sqrt{G/\rho_s}$ (Graff 2012). In load-free conditions, the interface propagates additional waves, confined to a narrow surface layer, studied by Lord Rayleigh (1885) and Love (1911), respectively. These two kinds of waves have two orthogonal polarisations, with the Rayleigh waves oscillating in the plane formed by the propagation direction (parallel to the undeformed surface) and the normal to the surface, whereas Love waves are shear waves oscillating along the surface and orthogonal to the propagation direction. An axisymmetric bubble collapse cannot induce Love waves and among the two possible polarisations of the (bulk) transverse waves, only the one oscillating in the axial plane is allowed.

The moving load adds even more features to the whole picture. Let us consider, for the sake of definiteness, the effect on the solid of a strong compression wave in the liquid on top of the liquid–solid interface. Such a wave will emanate radially from the region of bubble collapse, such that, under axisymmetry, its trace on the liquid–solid interface consists of an expanding circumference centred at the bubble's centre projection onto the surface. Being the fastest signal travelling in the liquid, outside this circumference the load applied to the solid vanishes altogether. Different cases may arise, depending on the relative speed of the liquid compression (load) wave and the longitudinal and the transverse elastic waves (also the additional parameter given by the speed of the Rayleigh wave should be taken into account, which is however very close to c_T). Without entering into detail here, the interaction of the loading wave with the surface produces an elastic wave locked to external disturbance. Moreover, the interaction of the longitudinal elastic

(bulk) wave with the liquid–solid surface generates a further wavefront, the so-called head, or von Schmidt, wave (Von Schmidt 1938). As we show, the amplitude of this interacting system of wavefronts is eventually modulated by the energy dissipation due to the plasticisation of the material taking place where the stress overcomes the material strength. Plasticity is a realm in itself. Here we stick to one of the most popular models, the so-called rate-independent classical plasticity model (Lubliner 2008).

The outline of the paper is as follows. Section 2 discusses the fluid–structure interaction and the approximation derived under the assumption of a stiff solid. Section 3 summarises the diffuse interface model, introducing the capillary distributed stress that complements the standard Navier–Stokes equations (mass, momentum and energy conservation) and illustrates the equation of state to account for the phase change. Section 4, for the convenience of unfamiliar readers, provides an account of the basic concepts of plasticity theory and elastoplastic waves. Section 5 presents a short description of the numerical methods adopted in the simulations. The main results concerning the dynamics of the collapsing bubble are reported in § 6 whereas the solid wall and related elastoplastic waves are addressed in § 7. Finally, conclusions are drawn in § 8 together with a discussion of perspectives and future research directions.

2. Fluid–solid interaction

The solid response to a bubble collapse is a typical example of fluid–structure interaction. Due to the nature of the solid material, it possesses certain peculiarities which are worth exploiting in the simulation. In fact, fluid and solid are coupled through the boundary conditions at the interface $\mathcal{I}$ which, assuming no overhangs, is described by the equation $z = h(x, y, t)$, where x, y and z are the three Cartesian coordinates of a point $\boldsymbol{x}$, with $z = 0$ the undeformed (planar) interface.

The fluid occupies the domain $\Omega_f = \{\boldsymbol{x} \in \mathbb{R}^3 : z > h(x, y)\}$, whereas the solid is confined to the complementary region $\Omega_s = \{\boldsymbol{x} \in \mathbb{R}^3 : z < h(x, y)\}$. The fluid is described in terms of the mass density $\rho(\boldsymbol{x}, t)$, the velocity $\boldsymbol{u}(\boldsymbol{x}, t)$ and the energy density $E(\boldsymbol{x}, t)$ fields which obey the fundamental conservation laws.

The solid is described by the density field $\rho_s(\boldsymbol{X}, t)$, the displacement field $\boldsymbol{r}(\boldsymbol{X}, t)$ and the energy density. Under isothermal conditions, the energy evolution is ignored in favour of the constant temperature assumption, thus rendering the Helmholtz free energy density $\hat{f}_S$ the thermodynamic potential of choice. Here, $\boldsymbol{X}$ is the Lagrangian coordinate providing the initial position of the solid continuum points such that $\boldsymbol{x} = \boldsymbol{X} + \boldsymbol{r}$. As is well known (Gurtin 1982), $\rho_s(\boldsymbol{X}, t) = \rho_0(\boldsymbol{X})$, while the displacement field obeys momentum conservation.

Apart from the initial state, the equations require boundary conditions that can be specified in terms of the fields or their (generalised) normal derivatives (i.e. traction vector and heat flux) at the boundary. In the present case, the domains change in time (free-boundary problem), and one should require the continuity of displacements and normal derivatives. This information is sufficient to determine the fields at the current time, in particular the velocity $\boldsymbol{u}_{\mathcal{I}} = \dot{\boldsymbol{r}}_{\mathcal{I}}$ which allows the interface to be updated according to the equation $h_t = \dot{z} - (\dot{x}h_x + \dot{y}h_y)$.

The specificity of the current problem is that the solid is stiff, meaning that its deformation (hence, also the interface displacement) is small under a finite intensity load, $|\boldsymbol{r}| = O(\epsilon) \ll 1$, where ϵ is a small parameter. In the simulations described in the following, this condition is accomplished by having a solid-to-liquid impedance ratio $Z_s/Z_l > 10.5$, such that the solid–liquid interface can be considered rigid. This assumption

allows linearising the entire system of equations with respect to the solid displacement while keeping finite all the other relevant quantities, in particular, the fluid velocity $\boldsymbol{u}$ and the stress distribution in the solid.

Linearisation of the solid's equations requires the stress tensor to be linearised with respect to the displacement field. Nevertheless, also in its linearised form, the stress in the solid is still large, implying that the material may yield under the load. The final result is a linear elastic model with plasticity occurring where the yield strength of the material is locally exceeded.

We stress that, from the point of view of the fluid, the system at order zero in ϵ still retains its original nonlinearity. To this order, the interface is flat and the no-slip condition applies in the form $\boldsymbol{u}_{\mathcal{I}} = 0$. In other words, the fluid motion decouples from the solid. As a consequence, the solid occupies its undeformed domain and experiences the load exerted by the fluid. Clearly, the solid displacement dictates the deformation of the interface. In principle, one may want to carry over this procedure to evaluate the effect on the fluid of the order one interface displacement. Although doable, this would be uninfluential if the first-order solution for the solid is sufficient.

3. Diffuse interface model of a cavitation bubble

The dynamics of a cavitation bubble close to a solid surface is described by a diffuse interface model (Jamet *et al.* 2001; Magaletti *et al.* 2015) which, overall, involves the familiar mass, momentum and energy conservation equations,

$$\frac{\partial \rho}{\partial t} + \boldsymbol{\nabla} \cdot (\rho \boldsymbol{u}) = 0, \tag{3.1a}$$

$$\frac{\partial \rho \boldsymbol{u}}{\partial t} + \boldsymbol{\nabla} \cdot (\rho \boldsymbol{u} \otimes \boldsymbol{u}) = \boldsymbol{\nabla} \cdot \boldsymbol{T}, \tag{3.1b}$$

$$\frac{\partial E}{\partial t} + \boldsymbol{\nabla} \cdot (E \boldsymbol{u}) = \boldsymbol{\nabla} \cdot (\boldsymbol{T} \cdot \boldsymbol{u}) - \boldsymbol{\nabla} \cdot \boldsymbol{q}_f, \tag{3.1c}$$

with $\boldsymbol{T}(\boldsymbol{x}, t)$ the stress tensor and $\boldsymbol{q}_f(\boldsymbol{x}, t)$ the energy flux. The specificity comes from the constitutive equations (Magaletti *et al.* 2016),

$$\boldsymbol{T} = -\left(p_0 - \frac{\lambda}{2} |\boldsymbol{\nabla} \rho|^2 - \rho \boldsymbol{\nabla} \cdot (\lambda \boldsymbol{\nabla} \rho) \right) \boldsymbol{I}$$
$$- \lambda \boldsymbol{\nabla} \rho \otimes \boldsymbol{\nabla} \rho + \eta (\boldsymbol{\nabla} \boldsymbol{u} + (\boldsymbol{\nabla} \boldsymbol{u})^{\mathrm{T}}) - \tilde{\eta} (\boldsymbol{\nabla} \cdot \boldsymbol{u}) \boldsymbol{I}, \tag{3.2}$$

$$\boldsymbol{q}_f = \lambda \rho \boldsymbol{\nabla} \rho \boldsymbol{\nabla} \cdot \boldsymbol{u} - k \boldsymbol{\nabla} \theta, \tag{3.3}$$

which, aside from classical effects described by Newton's law of viscosity and Fourier's law of heat conduction, accounts for distributed capillary terms depending on the density gradient. Moreover, a suitable pressure field is derived from an equation of state able to describe the thermodynamics of the fluid in the liquid, vapour and supercritical states that all occur during bubble implosion. In the above equations, the capillary coefficient $\lambda(\theta)$ is a function of the temperature θ, η is the first dynamic viscosity coefficient, $\tilde{\eta}$ (often taken to be $\tilde{\eta} = -2/3\eta$) is the second dynamic viscosity coefficient and k is the thermal conductivity.

Importantly, this system describes the transition from the high-density liquid to the low-density vapour, together with the change of the other thermodynamic and kinetic properties of the fluid. In the case of a vapour bubble in a liquid bulk, the fluid properties

switch smoothly across a thin interfacial layer, a distributed form of liquid–vapour interface as originally envisaged by van der Waals (1893). Its thickness is determined by the fluid thermodynamics,

$$\ell_{lv} = (\rho_l - \rho_v)\sqrt{\frac{\lambda/2}{w_0(\bar{\rho}) - w_0(\rho_v)}}, \tag{3.4}$$

where $\bar{\rho}$ is the fluid density where the density gradient is maximal, $|d\rho/dx|_{max} = \sqrt{2(w_0(\bar{\rho}) - w_0(\rho_v))/\lambda}$, and it is the seat of the strong density gradients that sum up to the (equilibrium) surface tension

$$\sigma = \int_{-\infty}^{+\infty} \lambda \left(\frac{d\rho}{dx}\right)^2 dx = \int_{\rho_v}^{\rho_l} \sqrt{2\lambda(w_0(\rho) - w_0(\rho_v))}\, d\rho, \tag{3.5}$$

where $w_0 = f_f^b - \rho\mu_f^b$, with f_f^b the fluid (bulk) Helmholtz free energy per unit volume and $\mu_f^b = \partial f_f^b/\partial\rho$ the chemical potential, which under equilibrium (saturation) conditions is a function of the only temperature ($\mu_f^b = \mu_{f\,eq}^b$).

The system of equations (3.1), complemented with the constitutive relations (3.2)–(3.3), is closed by prescribing the appropriate thermodynamics potential that holds across the liquid–vapour transition. Here the van der Waals equation of state for the Helmholtz free energy is assumed, $f_f^b/p_c = -8/3\rho_R\theta_R\{1 + \ln[(1 - \rho_R/3)/(\rho_c\rho_R\Lambda^3/m_p)]\} - 3\rho_R^2$, with the subscript R denoting reduced quantities (e.g. $\rho_R = \rho/\rho_c$), $\Lambda = \sqrt{2\pi\hbar^2/(m_p k_b\theta)}$ denoting the De Broglie thermal wavelength, m_p denoting the atom mass and the subscript c denoting the critical state. Hence, the pressure is

$$\frac{p_0}{p_c} = \frac{\rho^2}{p_c}\frac{\partial(f_f^b/\rho)}{\partial\rho} = \frac{8\rho}{3\rho_c - \rho}\frac{\theta}{\theta_c} - 3\left(\frac{\rho}{\rho_c}\right)^2. \tag{3.6}$$

Most of the boundary conditions are standard: in the present case, as discussed in §2, no-slip and impermeability conditions and constant temperature hold on the flat solid wall. A little more information is needed concerning capillarity, which should account for the solid wettability and requires explicitly calling into play the Helmholtz free energy functional for a stratified fluid, which reads

$$F[\rho, \theta] = \int_{\Omega_f} [f_f^b(\rho, \theta) + \lambda/2|\nabla\rho|^2]\, dV + \int_{\mathcal{I}} f_w(\rho, \theta)\, dS, \tag{3.7}$$

where $f_w(\rho, \theta) = -\cos\Theta \int_{\rho_v}^{\rho} \sqrt{2\lambda[w_0(\rho, \theta) - w_0(\rho_v, \theta)]}\, d\rho + \gamma_{sv}$ is the solid–fluid interfacial energy, with Θ Young's contact angle and γ_{sv} the surface energy for vapour in contact with the solid. In the free energy functional, the square density gradient term accounts for the excess energy of the interfacial layer and ultimately is the origin of the distributed capillary stresses. Minimising the free energy with respect to the density field provides two Euler–Lagrange equations. The first is the equation for equilibrium density, replaced here by the evolution equations illustrated before, whereas the second provides the boundary condition for the mass density (Gallo *et al.* 2021),

$$\lambda\frac{\partial\rho}{\partial n} + \frac{\partial f_w}{\partial\rho} = 0. \tag{3.8}$$

The flow is governed by three dimensionless parameters, the Cahn, Reynolds and Péclet numbers, taking the place of λ, $1/\eta$ and $1/k$, respectively, in (3.2) and (3.3),

999 A72-6

and defined as

$$Cn = \sqrt{\frac{\lambda \rho_c^2}{p_c R_0^2}}, \quad Re = \frac{R_0 \sqrt{p_c \rho_c}}{\eta}, \quad Pe = \frac{R_0 \sqrt{p_c \rho_c}}{k}, \qquad (3.9a\text{–}c)$$

with R_0 the initial bubble radius.

3.1. *Baroclinic vorticity production*

The interface and, possibly, the strong compression waves generated by the bubble implosion, may activate the baroclinic mechanism of vorticity production. As usual, the vorticity equation follows by taking the curl of the momentum equation (B26), rewritten here explicitly

$$\frac{\partial \rho \boldsymbol{u}}{\partial t} + \boldsymbol{\nabla} \cdot (\rho \boldsymbol{u} \otimes \boldsymbol{u}) = -\boldsymbol{\nabla} \left(p_0 - \frac{\lambda}{2} |\boldsymbol{\nabla} \rho|^2 - \rho \boldsymbol{\nabla} \cdot (\lambda \boldsymbol{\nabla} \rho) \right)$$
$$- \boldsymbol{\nabla} \cdot (\lambda \boldsymbol{\nabla} \rho \otimes \boldsymbol{\nabla} \rho) + \boldsymbol{\nabla} \cdot \boldsymbol{\Sigma}, \qquad (3.10)$$

where $\boldsymbol{\Sigma}$ is the classical viscous part of the stress tensor. The first two terms on the right-hand side of (3.10) are manipulated to yield

$$- \boldsymbol{\nabla} \left(p_0 - \frac{\lambda}{2} |\boldsymbol{\nabla} \rho|^2 - \rho \boldsymbol{\nabla} \cdot (\lambda \boldsymbol{\nabla} \rho) \right) - \boldsymbol{\nabla} \cdot (\lambda \boldsymbol{\nabla} \rho \otimes \boldsymbol{\nabla} \rho)$$
$$= -\boldsymbol{\nabla} p_0 + \frac{1}{2} \frac{\partial \lambda}{\partial \theta} |\boldsymbol{\nabla} \rho|^2 \boldsymbol{\nabla} \theta + \rho \boldsymbol{\nabla} [\boldsymbol{\nabla} \cdot (\lambda \boldsymbol{\nabla} \rho)]. \qquad (3.11)$$

Expressing p_0 in terms of the bulk (fluid) Helmholtz free energy $f_f^b(\rho, \theta)$ and chemical potential $\mu_f^b = \partial f_f^b / \partial \rho$ as $p_0 = \rho \mu_f^b - f_f^b$, its gradient takes the form

$$\boldsymbol{\nabla} p_0 = \rho \boldsymbol{\nabla} \mu_f^b + \mu_f^b \boldsymbol{\nabla} \rho - \frac{\partial f_f^b}{\partial \rho} \boldsymbol{\nabla} \rho - \frac{\partial f_f^b}{\partial \theta} \boldsymbol{\nabla} \theta = \rho \boldsymbol{\nabla} \mu_f^b + s_f^b \boldsymbol{\nabla} \theta, \qquad (3.12)$$

where the bulk entropy density is $s_f^b = -\partial f_f^b / \partial \theta$. Substituting (3.12) in (3.11) and back into (3.10), we get

$$\frac{\partial \rho \boldsymbol{u}}{\partial t} + \boldsymbol{\nabla} \cdot (\rho \boldsymbol{u} \otimes \boldsymbol{u}) = -\rho \boldsymbol{\nabla} [\mu_f^b - \boldsymbol{\nabla} \cdot (\lambda \boldsymbol{\nabla} \rho)]$$
$$+ \left(-s_f^b + \frac{1}{2} \frac{\partial \lambda}{\partial \theta} |\boldsymbol{\nabla} \rho|^2 \right) \boldsymbol{\nabla} \theta + \boldsymbol{\nabla} \cdot \boldsymbol{\Sigma}. \qquad (3.13)$$

After noting that the terms in brackets on the right-hand side can be written in terms of generalised entropy and chemical potential,

$$s_f = -\frac{\delta F}{\delta \theta} = s_f^b - \frac{1}{2} \frac{\partial \lambda}{\partial \theta} |\boldsymbol{\nabla} \rho|^2, \quad \mu_f = \frac{\delta F}{\delta \rho} = \mu_f^b - \boldsymbol{\nabla} \cdot (\lambda \boldsymbol{\nabla} \rho), \qquad (3.14a,b)$$

where the total Helmholtz free energy of the system is $F[\rho, \theta] = \int_V [f_f^b(\rho, \theta) + \lambda/2 |\boldsymbol{\nabla} \rho|^2] \, dV$ (van der Waals 1979), and exploiting mass conservation, (3.13) reads

$$\frac{\partial \boldsymbol{u}}{\partial t} + \boldsymbol{u} \cdot \boldsymbol{\nabla} \boldsymbol{u} = \frac{D \boldsymbol{u}}{D t} = -\boldsymbol{\nabla} \mu_f - \frac{s_f}{\rho} \boldsymbol{\nabla} \theta + \frac{1}{\rho} \boldsymbol{\nabla} \cdot \boldsymbol{\Sigma}. \qquad (3.15)$$
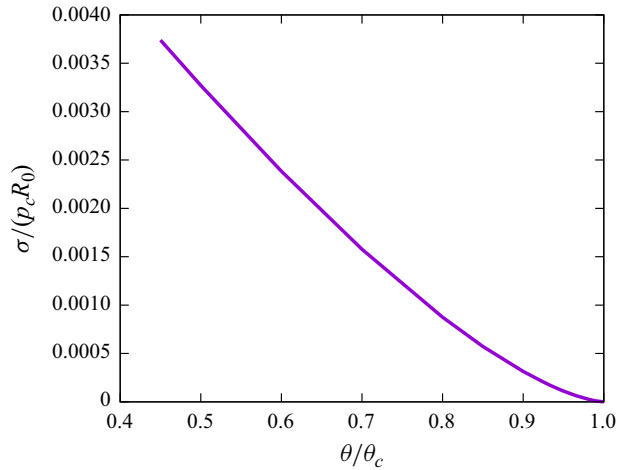
Figure 1. Surface tension σ vs temperature θ obtained from (3.5) with the Van der Waals equation of state. The capillary coefficient is kept constant corresponding to the dimensionless Cahn number $Cn = 1.1 \times 10^{-3}$, (3.9). In the graph, $p_c = 22$ MPa, $\theta_c = 647$ K and $R_0 = 10^{-6}$ m are the critical quantities and the reference radius used.

Applying the curl operator to (3.15), recalling that $Du/Dt = \partial u/\partial t + \nabla(|u|^2/2) + \zeta \times u$, the vorticity equation follows as

$$\frac{D}{Dt}\left(\frac{\zeta}{\rho}\right) = \left(\frac{\zeta}{\rho} \cdot \nabla\right) u - \frac{1}{\rho}\nabla\left(\frac{s_f}{\rho}\right) \times \nabla\theta + \frac{1}{\rho}\nabla \times \left(\frac{1}{\rho}\nabla \cdot \Sigma\right), \qquad (3.16)$$

where the first term on the right-hand side describes the stretching and tilting of vorticity, and the second is a generalised baroclinic term, responsible for vorticity production. It was shown in Gallo *et al.* (2018) that a constant capillary coefficient can reproduce the temperature dependence of the surface tension for a Lennard-Jones fluid; see figure 1 for the Van der Waals case. In these conditions, the baroclinic term appearing in (B27) simplifies considerably, see § 3.1.

A discussion of the sharp interface limit for the vorticity equation, which recovers the well-established sharp interface formulations (Magnaudet & Mercier 2020) (see also (Terrington, Hourigan & Thompson 2020, 2021, 2022) for a detailed analysis of vorticity generation on interfaces) compared with the diffuse interface form discussed here, is provided in Appendix B.

4. Elastoplastic dynamics of the substrate

It is a common belief that elastoplastic models may look bewildering to the non-specialist (Antman & Szymczak 1989). It may then be appropriate to simplify the discussion as much as possible to focus on key features. We henceforth assume that thermal effects can be neglected and we shall limit the analysis to materials with a rate-independent response. The first assumption is well-motivated given the small heat capacity of microbubbles as compared with the solid. Rate-independency, instead, is in principle questionable, due to the extremely fast time scales involved in the collapse. Nevertheless, we adopt a rate-independent model sufficiently rich to account for material hardening and to address the time-dependent elastoplastic response (Von Kármán & Duwez 1950). In case it

was required, the model, and the simulations thereof, can be readily extended in several respects to include thermal effects and rate-dependency, as we explain in Appendix A.

As discussed in § 2, for stiff materials the dynamics can be linearised with respect to the solid displacement. The formal procedure is highlighted in Appendix A which also provides a self-contained account of basic nonlinear plasticity elements. Here, as a necessary preliminary to elastoplastic wave dynamics, we begin the section with a concise summary of the equations, see Appendix A and (Antman 2005; Lubliner 2008) for further details.

Once linearised based on the assumption $|r| = O(\epsilon)$, § 2, the solid displacement field can be expressed in the Eulerian frame as $r = r(x, t)$ which, to the required accuracy level, entails $\rho_S(x, t) = \rho_0 + O(\epsilon)$, with $\rho_0 = $ const. for a homogeneous material. In the linearised theory, the (infinitesimal) strain reduces to

$$\boldsymbol{\epsilon} = (\nabla_x r + \nabla_x r^T)/2 \tag{4.1}$$

and possesses the peculiar property of being additively split into plastic and elastic parts, $\boldsymbol{\epsilon} = \boldsymbol{\epsilon}_p + \boldsymbol{\epsilon}_e$. With little surprise, the linearised momentum equation becomes

$$\rho_S \frac{\partial^2 r}{\partial t^2} = \nabla \cdot \boldsymbol{\sigma}, \tag{4.2}$$

where $\boldsymbol{\sigma} = C_e : \boldsymbol{\epsilon}_e$ is the (linearised) Cauchy stress, see Appendix A and, e.g. Gurtin, Fried & Anand (2010).

We assume the material to be isotropic, implying that the stress–strain relation involving the elastic tensor C_e is entirely characterised by the Lamé constants, λ_S and μ_S. When the material's distortional free energy density, $f_{dev}^e = \boldsymbol{\sigma}_{dev} : \boldsymbol{\sigma}_{dev}/(4\mu_S)$, is on the verge of exceeding the critical value $f_{dev}^c = \sigma_Y^2/(6\mu_S)$ that depends on the yield stress σ_Y, the material yields, the plastic strain accumulates and the material undergoes hardening. While all this is happening, the material will still remain in an admissible state, i.e. $f_{dev}^e - f_{dev}^c \leq 0$. This unilateral constraint acts only under plastic loading, i.e. when the two conditions (i) distortional free energy reaching the critical level, $|\boldsymbol{\sigma}_{dev}| = \sqrt{2/3}\sigma_Y$, and (ii) positive distortional stress power, $\boldsymbol{\sigma}_{dev} : \dot{\boldsymbol{\epsilon}} > 0$, are met.

The elastic strain, needed to evaluate the stress, is known from the total strain after the evolution equation for the plastic strain,

$$\dot{\boldsymbol{\epsilon}}_p = \begin{cases} \hat{\boldsymbol{\sigma}}_{dev} \otimes \hat{\boldsymbol{\sigma}}_{dev} : \dot{\boldsymbol{\epsilon}}/D & \text{if } |\boldsymbol{\sigma}_{dev}| = \sqrt{2/3}\sigma_Y \text{ and } \boldsymbol{\sigma}_{dev} : \dot{\boldsymbol{\epsilon}} > 0 \\ 0 & \text{otherwise,} \end{cases} \tag{4.3}$$

is solved, where $\hat{\boldsymbol{\sigma}}_{dev} = \boldsymbol{\sigma}_{dev}/|\boldsymbol{\sigma}_{dev}|$, $D = [1 + K_H/(3\mu_S)]$ and the strain rate is $\dot{\boldsymbol{\epsilon}} = (\nabla_x \dot{r} + \nabla_x \dot{r}^T)/2$. The symbol $\otimes$ denotes the tensor product and K_H is the hardening modulus (Lubliner 1972). The yield stress dictates the hardening. It is constant except under plastic loading when

$$\dot{\sigma}_Y = \sqrt{2/3} K_H |\hat{\boldsymbol{\sigma}}_{dev} : \dot{\boldsymbol{\epsilon}}|/D. \tag{4.4}$$

Strictly speaking, the system of ((4.2)–(4.4)) suffice to determine the elastoplastic evolution, once appropriate material parameters, boundary conditions on the fluid–solid interface and radiation conditions for the outward-propagating waves are prescribed. The accumulated plastic deformation, $\alpha_p \propto \int_0^t |\dot{\boldsymbol{\epsilon}}_p| \, dt$, is recovered from the yield stress, $\alpha_p = (\sigma_Y - \sigma_Y^0)/K_H$. The plastic dissipation differs from zero only under plastic loading where it is given by $\sqrt{2/3}\sigma_Y^0 |\hat{\boldsymbol{\sigma}}_{dev} : \dot{\boldsymbol{\epsilon}}|/D$.

Together with the capillary Navier–Stokes equations of § 3, this system is the basis for the simulations of the elastoplastic response to bubble collapse discussed in the forthcoming sections. Before proceeding, we take the chance to emphasise that all the relevant quantities are continuous across the plastic deformation boundary since they are linear in the distortional stress power that, together with the distortional free energy, demarcates the different regimes.

The elastoplastic dynamics is governed by the following dimensionless parameters:

$$c_L^* = c_L/\sqrt{p_c/\rho_c}, \quad c_T^* = c_T/\sqrt{p_c/\rho_c}, \quad \sigma_Y^{0*} = \sigma_Y^0/\mu_S, \quad K_H^* = K_H/(3\mu_S), \quad (4.5a\text{–}d)$$

where $c_L = \sqrt{(\lambda_S + 2\mu_S)/\rho_S}$ and $c_T = \sqrt{\mu_S/\rho_S}$.

4.1. *Elastoplastic waves*

Elastoplastic waves may develop within the material as a consequence of the loading exerted on the solid wall by the collapsing bubble. Considering for the moment the purely elastic case for which $\boldsymbol{\sigma}^e = \boldsymbol{C}_e : \boldsymbol{\epsilon}$, the Helmholtz decomposition for the displacement field $\boldsymbol{r}(\boldsymbol{x}, t) = \nabla\phi + \nabla \times \boldsymbol{A}$ (a vector in the r–z plane by axisymmetry) decouples (4.2) into two separate equations for the scalar, ϕ, and the vector potential, $\boldsymbol{A} = \psi\hat{\boldsymbol{e}}_z \times \hat{\boldsymbol{e}}_r$ (ψ is the analogous of the Stokes stream function),

$$\frac{\partial^2}{\partial t^2}(\nabla^2\phi) = c_L^2\nabla^2(\nabla^2\phi), \quad (4.6)$$

$$\frac{\partial^2}{\partial t^2}(\nabla^2\boldsymbol{A}) = c_T^2\nabla^2(\nabla^2\boldsymbol{A}), \quad (4.7)$$

where c_L and c_T are identified as the longitudinal and transverse wave propagation speeds, respectively. Equations (4.6) and (4.7) are, in fact, wave equations for the divergence and (the only non-vanishing component of) the curl of the displacement field ($\nabla^2\phi = \nabla \cdot \boldsymbol{r}, \; -\nabla^2\boldsymbol{A} = \nabla \times \boldsymbol{r}$). These two fields, which in isolation would describe purely longitudinal and transverse waves, respectively, interact with the wall and the moving load to generate a complex wave field (figure 2). In fact, the boundary condition on the wall,

$$\sigma_{zz}^e = \lambda_S\left[\frac{1}{r}\frac{\partial}{\partial r}(rr_r) + \frac{\partial r_z}{\partial z}\right] + 2\mu_S\frac{\partial r_z}{\partial z} = T_{zz}(r, t), \quad (4.8a)$$

$$\sigma_{rz}^e = \mu_S\left(\frac{\partial r_r}{\partial z} + \frac{\partial r_z}{\partial r}\right) = T_{rz}(r, t), \quad (4.8b)$$

where σ_{zz}^e (T_{zz}) and σ_{rz}^e (T_{rz}) are the normal and shear components of the elastic stress $\boldsymbol{\sigma}^e$ (fluid stress $\boldsymbol{T}$, § 3), respectively, once expressed in terms of scalar and vector potential ($r_r = \partial\phi/\partial r - \partial\psi/\partial z, \; r_z = \partial\phi/\partial z + 1/r\,\partial(r\psi)/\partial r$) couple together the two fields.

The sketch of figure 2 illustrates the elastic wavefronts generated by an axisymmetric compact pressure load, $T_{zz} = f(r - v_Dt), \; T_{rz} = 0$, suddenly applied to the wall at time $t = 0$ which travels radially outwards with velocity v_D intermediate between the speed of the longitudinal and the transversal elastic waves. At $t = 0$ longitudinal and transversal waves start being generated and are confined by hemispherical wavefronts whose configuration is depicted in the sketch at a later time t (blue and red circles, respectively). In the meanwhile, the disturbance moves and is found at time t somewhere between the traces on the wall of the longitudinal and transversal fronts. While the load moves, further waves are generated. Since it moves faster than the transversal wave system and slower than the longitudinal
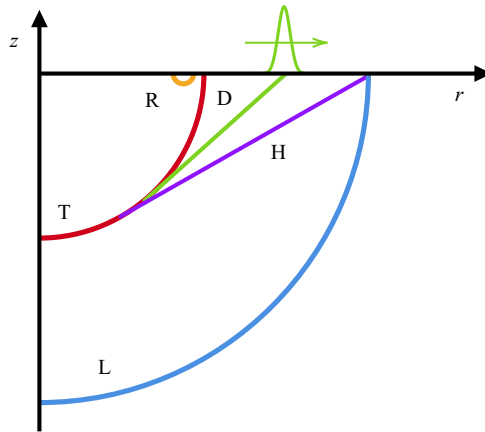
999 A72-10

Figure 2. A compact, axisymmetric pressure disturbance is suddenly applied at time $t = 0$ to the wall at the origin and spreads radially out. The elastic solid occupies the $z < 0$ half-space and the sketch concerns the case with a disturbance velocity intermediate between the faster longitudinal waves and the slower transversal waves. The disturbance (green), by moving faster than the transverse waves, gives rise to a conical wavefront (green line, D). The longitudinal waves move faster and are enveloped by their hemispherical wavefront impulsively generated at time $t = 0$ (blue line, L). The interaction of the longitudinal wavefront with the unloaded wall (ahead of the disturbance) causes the head wave (purple line, H). Behind the disturbance, the transversal wavefront produced at time $t = 0$, moves slower than the disturbance and is represented by the red line (T), followed by the Rayleigh wave, just behind, which is confined to the surface layer (yellow line, R).

one, at variance with the latter, the former cannot be radiated ahead of the disturbance. It remains confined to a cone whose generatrix is shown by the green oblique straight line tangent to the red circle forming the angle $\theta_D = \sin^{-1}(c_T/v_D)$ with the wall. The construction is the same as supersonic small disturbance theory in gas dynamics where one would talk of a Mach cone. Meanwhile, the longitudinal waves propagate ahead, where the wall is not yet perturbed by the pressure load. However, the field associated with the longitudinal waves alone cannot satisfy the load-free boundary conditions and, through the coupling implied by (4.8*a*), excites the transversal field. The corresponding wave system, being longitudinal waves supersonic with respect to transversal waves, must be confined within a second cone. This is called a head (or von Schmidt) (Von Schmidt 1938) wave and is shown by the oblique straight line in purple, which originates at the trace on the wall of the longitudinal front, is tangent to the red circle, and forms with the wall the angle $\theta_H = \sin^{-1}(c_T/c_L)$. Longitudinal and transverse systems are not the only free waves supported in this configuration. Actually, the unloaded wall sustains a third kind confined to the surface layer, the so-called Rayleigh waves. Their dispersion relationship, worked out as $(2 - c_R^2/c_T^2)^2 - 4(1 - c_R^2/c_L^2)^{1/2}(1 - c_R^2/c_T^2)^{1/2} = 0$ (Rayleigh 1885) and, for ductile metals, approximated by $c_R = 0.9194c_T$ (Graff 2012), shows that the Rayleigh wave is slower than all the others and localised in the region highlighted in yellow in the sketch. Other waves that could exist in principle (namely transverse wave and Love surface wave with polarisation normal to the axial plane shown in the sketch) are ruled out by the assumed symmetry of the problem. Once the general principle is laid down, it is easy to realise what to expect depending on the relative velocity of the load with respect to characteristic elastic speeds. Three cases are identified, (i) $v_D < c_T$, (ii) $c_L > v_D > c_T$ and (iii) $v_D > c_L$, as discussed in a series of beautiful papers in the late 1960s (Gakenheimer & Miklowitz 1969; Gakenheimer 1971); see also the book (Miklowitz 2012), where analytic function and integral transform theories are cleverly exploited.

Let us now turn our attention to the elastoplastic case. For an elastoplastic material, Appendix A, (4.6) and (4.7) take the form

$$\left(\frac{\partial^2}{\partial t^2} - c_L^2 \nabla^2 \right) \nabla^2 \phi = -2c_T^2 (\nabla \otimes \nabla) : \boldsymbol{\epsilon}_p, \tag{4.9}$$

$$\left(\frac{\partial^2}{\partial t^2} - c_T^2 \nabla^2 \right) \nabla^2 \boldsymbol{A} = 2c_T^2 \nabla \times (\nabla \cdot \boldsymbol{\epsilon}_p), \tag{4.10}$$

where the plastic deformation, time-dependent in general, $\boldsymbol{\epsilon}_p(\boldsymbol{x}, t)$, follows by solving (4.3), where the strain rate in terms of the time derivative of the potentials is $\dot{\boldsymbol{\epsilon}} = \nabla \otimes \nabla \dot{\phi} + [\nabla \otimes (\nabla \times \dot{\boldsymbol{A}}) + \nabla \otimes (\nabla \times \dot{\boldsymbol{A}})^{\mathrm{T}}]/2$, with $\dot{\phi}$ and $\dot{\boldsymbol{A}}$ the corresponding velocity potentials, $\boldsymbol{v} = \dot{\boldsymbol{r}} = \nabla \dot{\phi} + \nabla \times \dot{\boldsymbol{A}}$. Equations (4.9), (4.10) involve wave operators on the left-hand side and memory terms on the right-hand side which come from the time-integration of (4.3). Note that the right-hand side of (4.3) is nonlinear in the fields, given the dependency of $\boldsymbol{\sigma}_{dev}$ on the solution.

To qualitatively describe the rich phenomenology implied by the elastoplastic model, we may consider two limiting conditions, one concerning a system remaining in the elastic range, $\dot{\boldsymbol{\epsilon}}_p = 0$, with preexistent plastic deformation, the other a system undergoing plastic loading, $\dot{\boldsymbol{\epsilon}}_p \neq 0$. In the first case, the plastic strain is time-independent, $\boldsymbol{\epsilon}_p(\boldsymbol{x})$, and the potentials can be split into time-independent and transient components, $\phi = \phi^p(\boldsymbol{x}) + \phi_w^e(\boldsymbol{x}, t)$, $\boldsymbol{A} = \boldsymbol{A}^p(\boldsymbol{x}) + \boldsymbol{A}_w^e(\boldsymbol{x}, t)$, where the equations

$$c_L^2 \nabla^4 \phi^p = 2c_T^2 (\nabla \otimes \nabla) : \boldsymbol{\epsilon}_p, \tag{4.11}$$

$$c_T^2 \nabla^4 \boldsymbol{A}^p = -2c_T^2 \nabla \times (\nabla \cdot \boldsymbol{\epsilon}_p), \tag{4.12}$$

completed with load-free boundary conditions account for the deformation induced in the solid by the preexistent plastic region with the residual stress given by $\boldsymbol{\sigma}_R = \boldsymbol{C}^e : (\boldsymbol{\epsilon} - \boldsymbol{\epsilon}_p)$. The transient contributions, ϕ_w^e, $\boldsymbol{A}_w^e$, obey the very same equations and boundary conditions of the previously considered purely elastic case, implying that the wave propagation is not altered.

The second case can be addressed in the same spirit, after assuming, for the purpose of the present analysis, the plastic strain field $\boldsymbol{\epsilon}_p(\boldsymbol{x}, t)$ to be known. Now the splittings read $\phi = \phi^p(\boldsymbol{x}, t) + \phi_w^e(\boldsymbol{x}, t)$ and $\boldsymbol{A} = \boldsymbol{A}^p(\boldsymbol{x}, t) + \boldsymbol{A}_w^e(\boldsymbol{x}, t)$, where the elastic wave components behave as before and take care of the load at the interface, whereas the potentials ϕ^p and $\boldsymbol{A}^p$ obey the forced wave equations

$$\left(\frac{\partial^2}{\partial t^2} - c_L^2 \nabla^2 \right) \nabla^2 \phi^p = -2c_T^2 (\nabla \otimes \nabla) : \boldsymbol{\epsilon}_p, \tag{4.13}$$

$$\left(\frac{\partial^2}{\partial t^2} - c_T^2 \nabla^2 \right) \nabla^2 \boldsymbol{A}^p = 2c_T^2 \nabla \times (\nabla \cdot \boldsymbol{\epsilon}_p), \tag{4.14}$$

with load-free boundary conditions. The nature of the solutions to the above equations depends on the behaviour of the plastic strain field. In fact, it is known that, under suitable conditions, elastoplastic waves can develop (Antman & Szymczak 1989; Lubliner 2008). In this case, the potentials inherit the propagative nature of the plastic strain field plus a system of purely elastic waves. Combining the partial solutions together, we arrive at a displacement field that possesses wave characteristics, in part purely elastic and in part associated with the envisaged elastoplastic propagation.

5. Numerical methods

The Navier–Stokes equations with capillarity (3.1) with constitutive equations (3.2), (3.3), and the elastoplasticity equations (4.2), (4.3) are solved adopting the finite-element method, implemented using the deal.II library (Arndt *et al.* 2023).

Concerning the fluid, an auxiliary field $g = \nabla^2 \rho$ is added to take into account higher-order derivatives in the stress tensor (3.2). Piecewise linear shape functions have been selected for the spatial discretisation, and the fluid domain Ω_f is subdivided in two regions with different spatial resolution. A finer grid is adopted around the bubble initial position and in proximity to the wall, extending radially to follow the propagation of the shock wave at the wall, whereas a coarser grid is used far from the bubble. The grid size in the former region is $\Delta = 20R_0/2^{11}$, with R_0 the initial bubble radius ($20R_0$ being the domain extension in both directions), whereas in the latter the grid size is $\Delta = 20R_0/2^6$. To properly resolve the gradients at the interface, at the shock wave fronts, and near the solid wall an automatic grid refinement based on the Kelly error estimator (Kelly *et al.* 1983; Ainsworth & Oden 2011) is employed, using the density gradients as indicator and setting the minimum allowed grid size to $\Delta = 20R_0/2^{15}$. For time discretisation, the second-order Crank–Nicolson scheme is adopted, with timestep Δt in the range 10^{-5}–$10^{-3} \, t_{ref}$, depending on the collapse dynamics. System nonlinearities are treated with a Newton–Raphson iterative method.

Regarding the elastoplastic solid, the domain Ω_s (here the extension is reduced to $10R_0$ in both directions, exploiting an absorbing layer to prevent spurious reflections, to focus on the local wave structure) is discretised with a uniform grid with grid size $\Delta = 10R_0/2^{11}$. The second-order Newmark-beta method (Newmark 1959) is used for time discretisation with parameters $\beta = 0.49$ and $\gamma = 0.9$, and timestep $\Delta t \leq 0.9\Delta / \max(c_L, v_D)$, with c_L and v_D the longitudinal waves speed and the disturbance speed at the wall, respectively. The nonlinearities arising due to plasticity effects are treated with the Newton–Raphson iterative method, and the local plastic equilibrium is ensured with a classical return mapping algorithm (Simo & Taylor 1985; Simo & Hughes 2006). As anticipated, viscous layers are used to dampen outward-propagating waves and avoid spurious reflections at the artificial boundaries.

The code was validated against finite-difference codes already used in a previous work (Magaletti *et al.* 2016), and a convergence analysis has been carried out to ensure the results are grid-independent, by increasing the maximum resolution of the fluid grid in the interfacial region setting $\Delta = 20R_0/2^{16}$.

Additional details regarding the numerical methods are provided in the see supplementary material available at https://doi.org/10.1017/jfm.2024.925.

6. Bubble dynamics

In experiments on single bubbles, the bubble is usually generated by a spark or laser (Lauterborn & Bolle 1975; Sinibaldi *et al.* 2019), that is, it is formed due to intense electric fields that induce the dielectrics breakdown in the form of hot plasma. This leads to the localised vaporisation of the water and ultimately initiates the bubble. After its formation, the bubble expands up to a maximum radius, collapses back, rebounds and is finally reabsorbed. Although the energy deposition process can be simulated (Abbondanza, Gallo & Casciola 2023*b*), the cases analysed here consider instead a preexisting bubble of a given radius and let it collapse as a result of an overpressure in the liquid.

6.1. *Simulation set-up*

All the simulations are performed using cylindrical coordinates r, θ and z, in the truncated domain $\Omega_f = [0, R] \times [0, 2\pi] \times [0, H]$, assuming axisymmetry. On the solid wall, located at $z = 0$, the boundary conditions prescribe

$$\boldsymbol{u} = 0, \quad \boldsymbol{q}_f \cdot \hat{\boldsymbol{e}}_z = 0, \quad -\lambda \frac{\partial \rho}{\partial z} + \frac{\partial f_w}{\partial \rho} = 0 \quad \text{on } z = 0, \quad (6.1a\text{--}c)$$

with $-\hat{\boldsymbol{e}}_z$ the outward normal at the adiabatic wall, where no-slip is assumed and the last equation determines the contact angle (3.8). The remaining part of the domain boundary is assumed sufficiently far from the bubble to allow the boundary conditions,

$$\boldsymbol{u} = 0, \quad \boldsymbol{q}_f \cdot \hat{\boldsymbol{n}} = 0, \quad \frac{\partial \rho}{\partial n} = 0 \quad \text{on } z = H \text{ or } r = R. \quad (6.2a\text{--}c)$$

The initial conditions are

$$\rho(r, z, 0) = \rho_v^{eq} + \frac{1}{2} \left(1 + \tanh \left(\frac{\sqrt{r^2 + (z - Z_c)^2} - R_0}{\ell} \right) (\rho_l - \rho_v^{eq}) \right), \quad (6.3)$$

$$\boldsymbol{u}(r, z, 0) = \boldsymbol{0}, \quad (6.4)$$

$$\theta(r, z, 0) = \theta_0, \quad (6.5)$$

with ρ_v^{eq} and ρ_l the initial vapour and liquid density, respectively. The initial condition describes a still vapour bubble of radius R_0, at the external liquid temperature θ_0, with the centre on the symmetry axis and standoff distance Z_c with respect to the wall, see the sketch in figure 3(*a*). Here $\ell \simeq \ell_{LV}$, (3.4), is the initial width of the liquid–vapour interface. As is well known (Debenedetti 2021), a bubble in an unbound domain cannot exist in a stable equilibrium state. In fact, the thermal, mechanical and chemical equilibria,

$$\theta = \theta_0, \quad p_v^{eq}(\rho_v^{eq}, \theta_0) - p_l^{eq}(\rho_l^{eq}, \theta_0) = \frac{2\sigma}{R_0}, \quad \mu_f^b(\rho_l^{eq}, \theta_0) = \mu_f^b(\rho_v^{eq}, \theta_0), \quad (6.6a\text{--}c)$$

lead to a critical bubble that would either spontaneously shrink (be reabsorbed into the liquid) or expand. Starting from the unstable state described by (6.6), the increase of the liquid density to $\rho_l > \rho_l^{eq}$ invariably leads to collapse of the bubble.

Figure 4 shows the equilibrium liquid pressure at temperature θ_0 as a function of the bubble radius. It is substantially independent of the bubble size as soon as the bubble radius is 10 µm or larger. According to the Rayleigh–Plesset dynamics (Brennen 2014), in free space, the collapse time of a vapour bubble of radius R_0 is approximately given by

$$T_c(R_0) = R_0 \sqrt{\frac{3\rho_l}{2(p_l - p_v^{eq})}} \int_0^1 dx \sqrt{\frac{x^3}{1 - x^3 + \alpha(1 - x^2)}}, \quad (6.7)$$

where $x = R/R_0$, $\alpha(R_0) = 3\sigma/[R_0(p_l - p_v^{eq})]$, $p_l = p_l^{eq}(1 + \beta)$ and $\rho_l = \rho_l(\theta_0, p_l)$, with $\beta = (p_l - p_l^{eq})/p_l^{eq}$ the overpressure parameter quantifying the liquid pressure increase over the equilibrium value given by (6.6). The approximation consists of assuming that the liquid state, that is pressure and density, is not affected by the bubble collapse and the vapour pressure remains at the equilibrium value. It is worth stressing that the above prediction accounts for the presence of surface tension which becomes significant
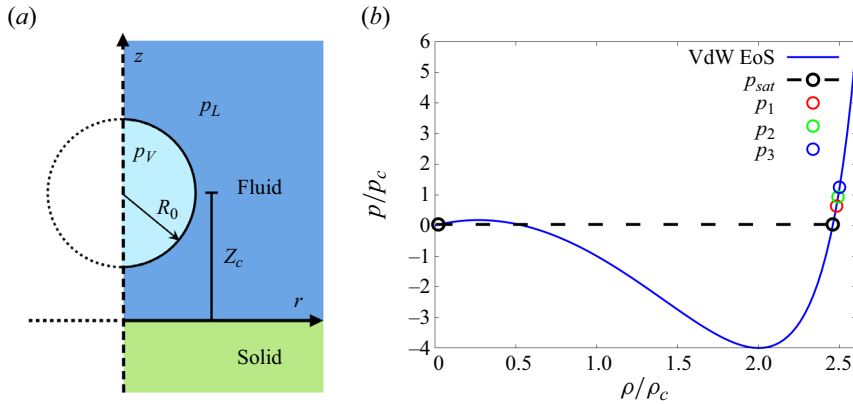
999 A72-14

Figure 3. (*a*) Initial two-dimensional cylindrical configuration in the fluid domain. The bubble is initially located on the axis, at height Z_c. The pressure in the liquid is p_L, whereas the pressure in the bubble is p_V. (*b*) Initial overpressure conditions in the liquid represented on a normalised p–ρ plane, with the corresponding van der Waals equation of state at the initial temperature of the system. Colours correspond to the three different conditions explored, increasing overpressure from red to blue. The saturation pressure, very similar to the equilibrium pressure in these conditions, is represented with a dashed line. Here $p_c = 22$ MPa and $\rho_c = 322$ kg m^{-3} are the critical pressure and density.
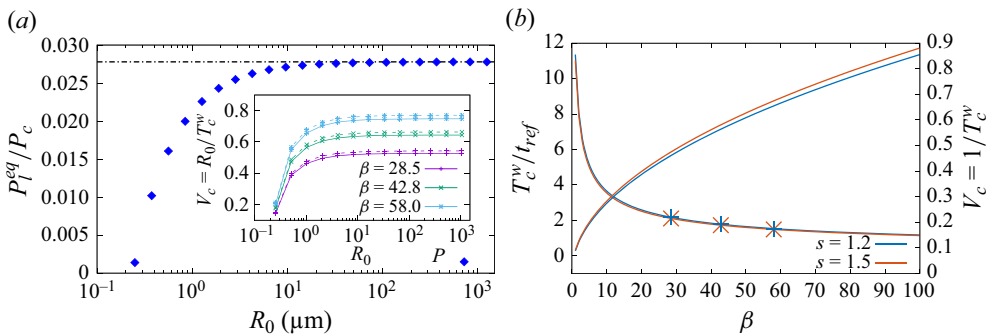
Figure 4. (*a*) Equilibrium liquid pressure, p_l^{eq}, blue symbols, vs initial bubble radius R_0. Inset: bubble collapse velocity V_c vs R_0 for different overpressure parameter β and two values of the standoff distance parameter ($s = 1.2$ and 1.5, solid and dashed lines, respectively). (*b*) Collapse time (left axis) and collapse velocity (right axis) vs β for two standoff distances, for the case with $R_0 = 1$ µm. The (partially superimposed in twos) symbols denote the conditions for the six simulations analysed in the following. The corresponding collapse times for $s = 1.2$ are $T_c^W/t_{ref} = 2.17$, 1.77 and 1.53 for $\beta = 28.5$, 42.8 and 58.0, respectively. The three figures change to $T_c^W/t_{ref} = 2.10$, 1.72 and 1.48 for $s = 1.5$.

for microbubbles. From the collapse time, one may define a typical collapse speed, $V_c = R_0/T_c$ that is also found to be substantially independent of the bubble radius above $R_0 = 10$ µm (figure 4). With respect to this, one may assume 10 µm as the size below which the vapour cavity can be considered a microbubble.

For future convenience, we anticipate that the collapse time for a bubble close to a solid surface may be obtained by multiplying (6.7) by the factor $1 + 0.205/s$, $T_c^w(R_0, s) = T_c(R_0)(1 + 0.205/s)$ where $s = Z_c/R_0$ (Rattray 1951; Plesset & Chapman 1971).

Dealing with microbubbles, in the simulations, the initial radius and equilibrium temperature are set to $R_0 = 1$ µm and $\theta_0 = 0.5\,\theta_c$, whereas the equilibrium densities follow from (6.6) which, for a van der Waals fluid (3.6), provide $\rho_v^{eq} \approx \rho_v^{sat} = 0.022\,\rho_c$

999 A72-15

(*a*)

$t/T_c^w = 0$ $t/T_c^w = 0.85$ $t/T_c^w = 0.96$ $t/T_c^w = 1.02$

(*b*)

$t/T_c^w = 1.13$ $t/T_c^w = 1.24$ $t/T_c^w = 1.36$ $t/T_c^w = 1.58$
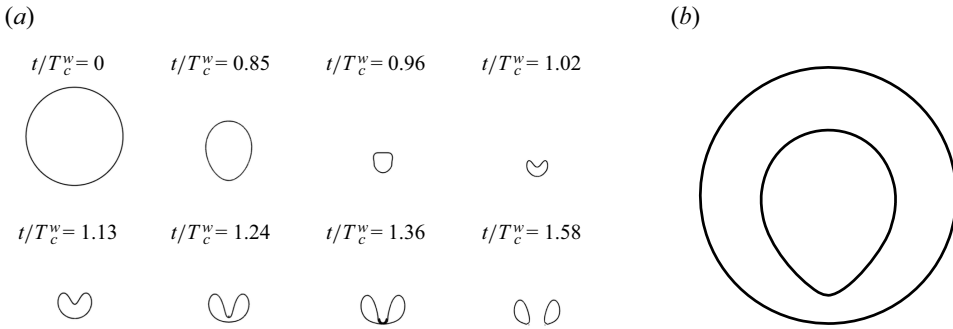
Figure 5. (*a*) Bubble topology during the collapse ($\beta = 42.8$, $s = 1.2$). Snapshots are taken at different times, and the solid line is the critical density isocontour. (*b*) Early bubble deformation stage modelled by potential flow theory and method of images.

and $\rho_l^{eq} = 2.458\rho_c$. For such a bubble, the vapour is practically at saturation conditions, whereas the liquid is slightly metastable. Six configurations were examined with $Re = 83.5$, $Cn = 1.1 \times 10^{-3}$ and $Pe = 14.9$ at changing the overpressure, $\beta \approx 28.5$, 42.8 and 58.0, and the standoff distance $s = 1.2$ and 1.5; see figure 3(*b*).

In the following, all quantities are made dimensionless with respect to the reference values $\theta_c = 647$ K, $p_c = 22$ MPa, $\rho_c = 322$ kg m^{-3}, $v_{ref} = \sqrt{p_c/\rho_c}$ m s^{-1} and $t_{ref} = R_0/v_{ref}$ s.

6.2. *Bubble topology, liquid jet and shock waves*

It is known that although a bubble in free space could, in principle, keep the spherical symmetry while shrinking, strong instabilities arise that prevent achieving perfectly symmetric collapse (Brenner, Hilgenfeldt & Lohse 2002). In fact, the solid wall breaks the spherical symmetry from the collapse outset, leading to a fast liquid jet that pierces the bubble, as confirmed by several experimental and numerical works (Lauterborn & Bolle 1975; Johnsen & Colonius 2009; Magaletti *et al.* 2016; Zeng *et al.* 2018; Lechner *et al.* 2020; Saade, Lohse & Fuster 2023), and produces the rearrangement from spherical to toroidal topology; see figures 5 and 6 where the bubble shape is conventionally identified by the critical density isocontour. As discussed later, during the collapse, the fluid locally overcomes the critical temperature, whereas the density progressively becomes supercritical. The two simulations at different standoff distance confirm (Philipp & Lauterborn 1998) that this parameter strongly influences the collapse. Indeed, the topology change, which is hardly achieved for $s = 1.5$, see figure 6(*a*), is apparent in figure 5(*a*) for $s = 1.2$.

During the early stages of the collapse, while shrinking, the bubble becomes egg-shaped. As shown in figures 5(*b*) and 6(*b*), this behaviour is largely explained by the blockage effect of the wall that, in essence, can be described using potential flow theory combined with the method of images (Plesset & Chapman 1971). The evolution of bubble volume, as identified by the critical density contour, is reported in figure 7 which shows that the first collapse time almost perfectly coincides with the estimate T_c^w.

Figure 8 illustrates the events occurring during the early collapse stage and reports density and temperature isocontours with superimposed velocity field (arrows) and the critical density and temperature isolevels (solid lines). The process is initiated by the asymmetric velocity distribution generated by the blockage of the solid wall that leads

999 A72-16

(*a*)   (*b*)

$t/T_c^w = 0$ $t/T_c^w = 0.82$ $t/T_c^w = 0.93$ $t/T_c^w = 1.05$

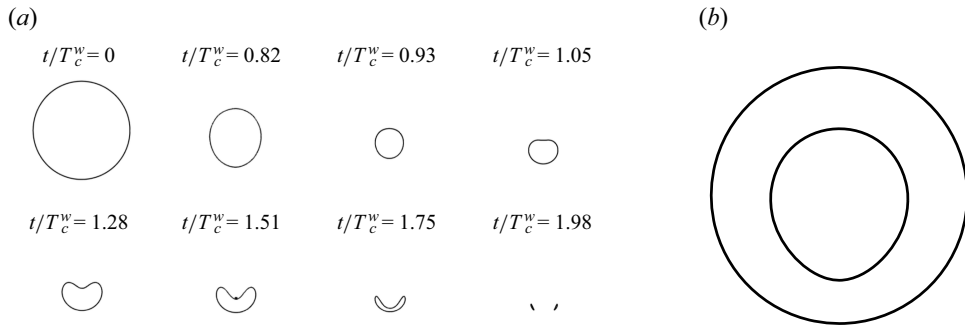$t/T_c^w = 1.28$ $t/T_c^w = 1.51$ $t/T_c^w = 1.75$ $t/T_c^w = 1.98$

Figure 6. Bubble topology evolution ($\beta = 42.8$, $s = 1.5$) and early bubble deformation stage modelled by potential flow theory and method of images, as in figure 5.
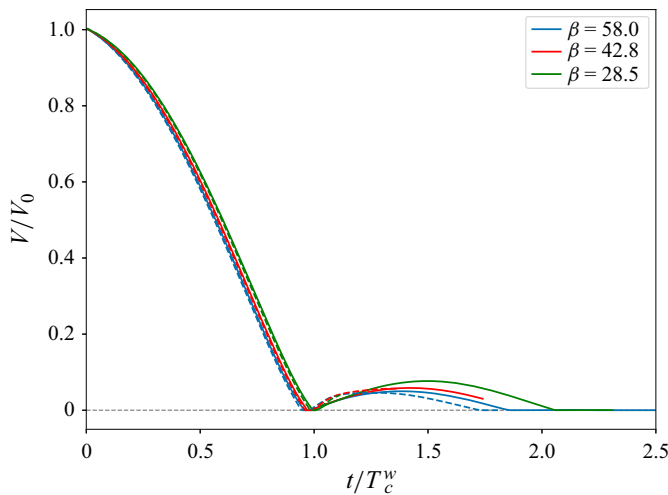
Figure 7. Bubble volume vs time for different overpressure β and standoff distance s (solid and dashed lines correspond to $s = 1.2$ and 1.5, respectively).

to faster speed on the bubble distal part. The temperature progressively increases until, in figure 8(*c*), the vapour becomes supercritical, hence incondensable, in the bubble core. Due to the velocity difference between the distal and proximal parts of the bubble, the bubble overall translates toward the wall. It turns out that in the reference frame of the bubble centre-of-figure, the relative velocity compressing the bubble is larger on the sides than on the top and bottom. As a consequence, while the bubble shrinks, its overall shape is turned from an initial sphere into an ovoid with the major axis normal to the wall.

Figure 9 displays the pseudo-Schlieren field (the exponential of the density gradient magnitude that is the better-suited observable to identify the bubble boundary) at a sequence of selected instants along the collapse process for the case with $\beta = 58.0$ and $s = 1.2$. Note that the time intervals between frames are not equispaced, with a much smaller time interval in the region between the end of the first collapse and the beginning of the first rebound where the bubble volume plateaus to zero in a small time interval around $t/T_c^w = 1$, hardly visible on the scale of figure 7. During the first phase, left column, the bubble volume shrinks, and a compression wave propagates inside the bubble towards the wall. The wavefront separates the bubble interior into two parts, with the lower
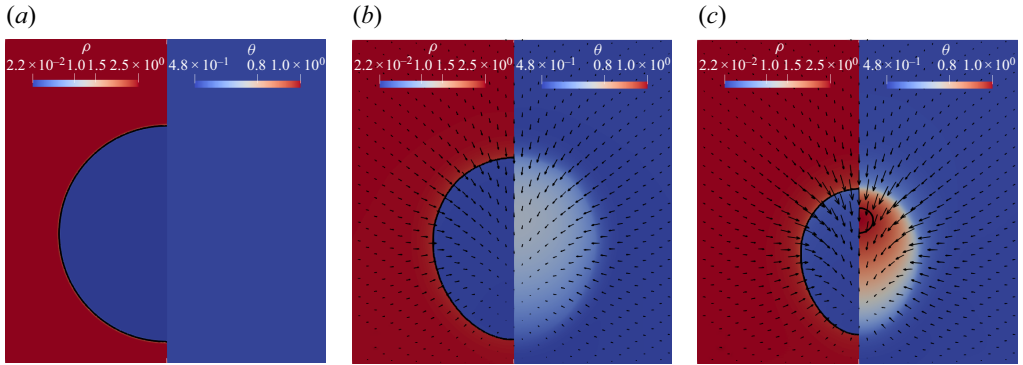
Figure 8. Early stages of the bubble collapse. Density and temperature are depicted as coloured isocontour lines in the left and right half of each panel, respectively, $t/T_c^w = 0$, 0.59 and 0.79 for panels (*a*), (*b*) and (*c*), respectively. The velocity field is shown by the vectors. The solid line in panel (*c*) is the critical temperature isoline, and the fields are expressed dimensionless with respect to the critical values $\rho_c = 322$ kg m^{-3} and $\theta_c = 647$ K.

part relatively still ($t/T_c^w = 0.93$). Noticeably, the volume enclosed by the critical density isocontour shrinks much faster than the region enveloped by the sharp density gradients that in fact represent the boundary demarcating the region of lower density, inside, from the higher density, outside. This difference should be kept in mind while interpreting the result on the bubble volume. While the wave propagates, it starts interacting with the exterior fluid through the density interface ($t/T_c^w = 0.95$). In fact, the pressure wave propagating in the bubble interior is refracted at the density interface exciting the exterior wave and the wave reflected towards the interior; see e.g. Henderson (1989) for a related case of shock wave refraction across a sharp density interface and Ranjan, Oakley & Bonazza (2011) for a comprehensive analysis on shock–bubble interactions. The vectors clearly indicate that all the configurations in the left column of the figure correspond to liquid moving towards the bubble, consistently with an implosive phase of the dynamics.

The series of events taking place when the incident wave reaches the bottom of the bubble is provided in detail in figure 10, for the same case with $\beta = 58.0$ and $s = 1.2$. While the wave is refracted across the density interface at the bottom of the bubble, the reflected wave focuses on the axis ($t/T_c^w = 0.962$). This leads to a further reflection that produces the spherical wave emerging from the bottom interface and expanding within the bubble. Simultaneously, the refracted wave in the bubble exterior is also focused on the axis to generate the spherical compression wave expanding under the bubble interface ($t/T_c^w = 0.97$). This wave is responsible for the liquid velocity diverging from the bubble, initiating the rebound phase apparent in the centre column of figure 9 ($t/T_c^w = 1.0$–1.25). During this phase, a jet pierces the bubble changing its topology from spheroidal to toroidal to eventually impinge the wall, as shown in the right column of the figure.

During the collapse, the volume enclosed by the critical density shrinks to zero, but a region of incondensable fluid survives. Figure 11 shows the evolution of the volume where $\theta \geq \theta_c$ compared with that where $\rho \leq \rho_c$. Around the collapse time, the region of supercritical temperature encloses that where the density is subcritical. It turns out that, for most of the evolution, the critical density isoline is a good representative of the bubble. However, when the fluid gets supercritical, this correspondence is lost, confirming that the results are more precisely represented in terms of the numerical Schlieren, which better corresponds to optics experiments.
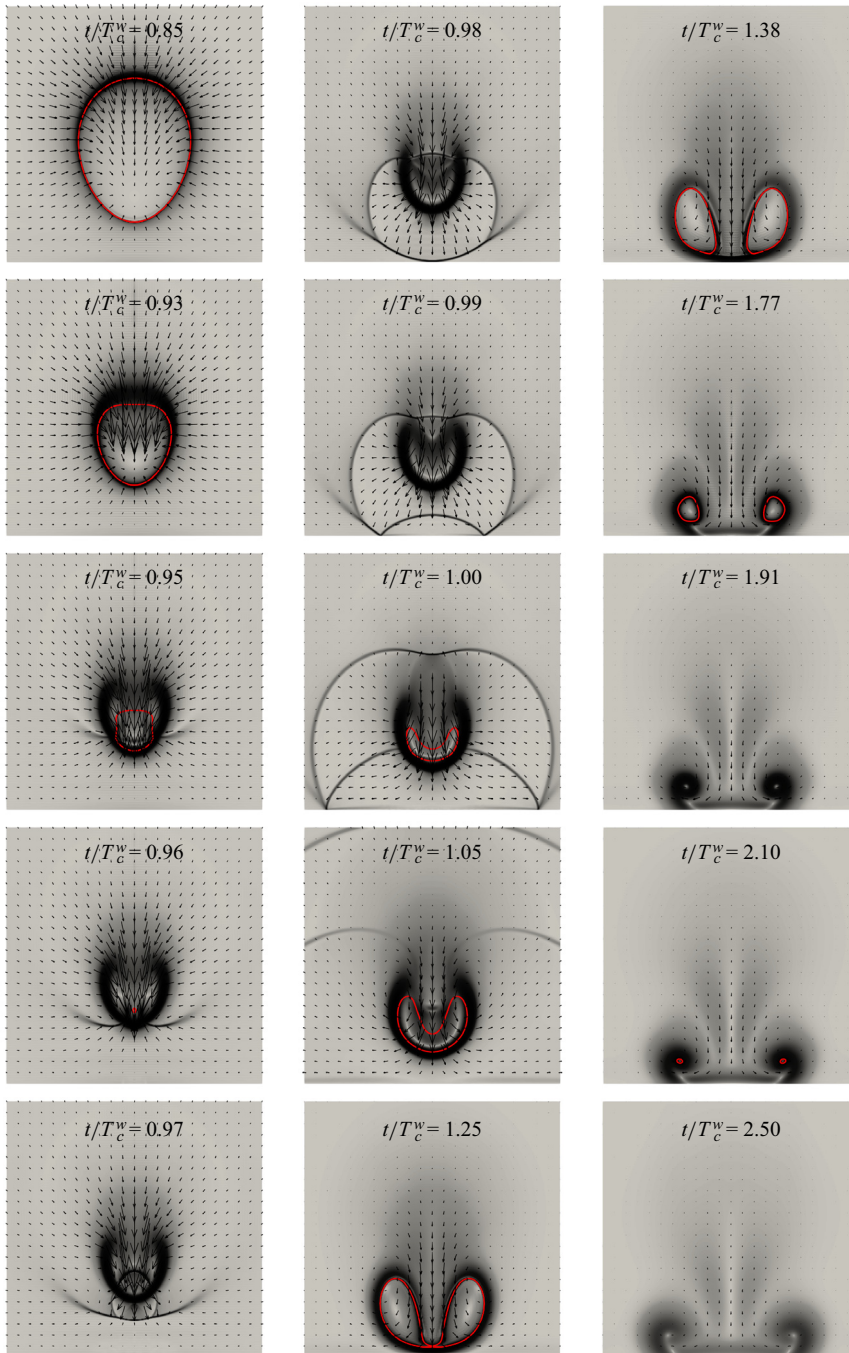
999 A72-18

Figure 9. Collapse of a vapour bubble near a solid wall, $\beta = 58.0$, $s = 1.2$. Schlieren-like representation of the density gradients with the superimposed velocity field. The red solid line is the density iso-contour $\rho = \rho_c$ used to evaluate the bubble volume in figure 7.
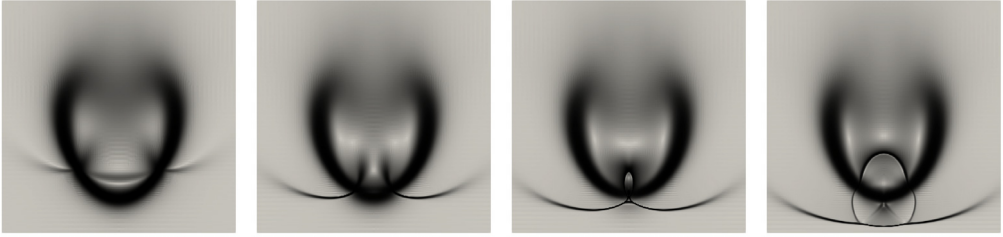
Figure 10. Schlieren-like representation of the density gradients, showing the density interface across the bubble boundary and the primary shock wave propagating inside the bubble with refracted and reflected shock waves, $\beta = 58.0$, $s = 1.2$. From left to right: $t/T_c^w = 0.950, 0.959, 0.962$ and 0.965.
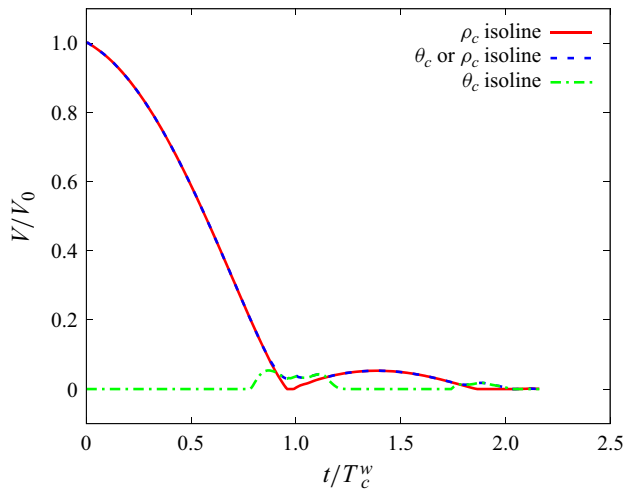
Figure 11. History of the volume enclosed by the critical density isoline (solid line, volume where $\rho \leq \rho_c$) and by the temperature isoline (dash-dotted line, volume where $\theta \geq \theta_c$). The dashed line is the volume of the region where either $\rho \leq \rho_c$ or $\theta \geq \theta_c$. Here $\beta = 58.0$, $s = 1.2$.

6.3. *Bubble vorticity*

The change in the bubble topology from spherical to toroidal is accompanied by the formation of a jet and circulatory motions clearly seen in the vector velocity fields in figure 9. They are the clear signature of vorticity that is generated during the collapse phase. For the present van der Waals equation of state, the baroclinic vorticity generation term derived from the capillary Navier–Stokes equation in § 3.1 is given by

$$B = -\frac{1}{\rho}\boldsymbol{\nabla}\left(\frac{s_f}{\rho}\right)\times\boldsymbol{\nabla}\theta = -\frac{1}{\rho}\frac{\partial s_f^b/\rho}{\partial\rho}\boldsymbol{\nabla}\rho\times\boldsymbol{\nabla}\theta = \frac{8}{\rho^2(3-\rho)}\boldsymbol{\nabla}\rho\times\boldsymbol{\nabla}\theta, \qquad (6.8)$$

where the expression in the middle exploits a constant capillary coefficient. We recall that the above expression is dimensionless, with the corresponding dimensional quantity obtained after multiplying by $p_c/(\rho_c^2 R_0^2)$. Many physical mechanisms may contribute to vorticity generation as described in the context of a sharp interface model; see e.g. Magnaudet & Mercier (2020); Terrington *et al.* (2022) for a detailed discussion and Appendix B for the derivation of the sharp interface limit from the present formulation). For constant viscosity, all of them are included in the diffuse interface form of the baroclinic term.
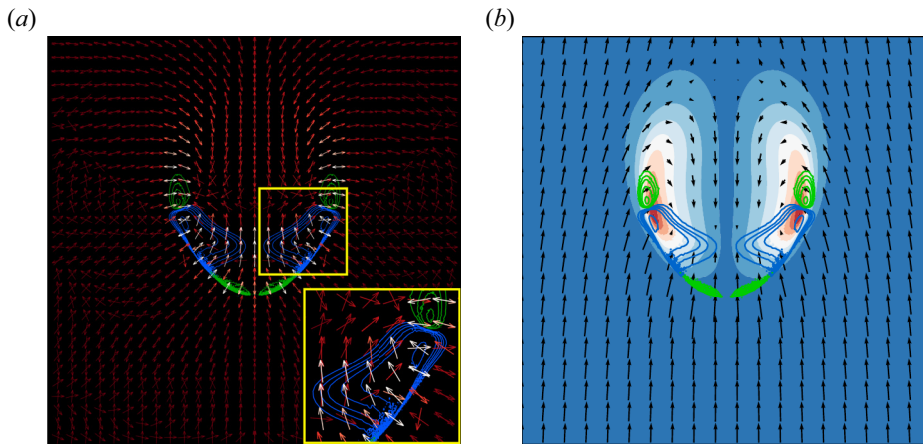
999 A72-20

(a) (b)

Figure 12. Vorticity production and transport, $t/T_c^w = 0.94$, $\beta = 58.0$ and $s = 1.2$. (a) Isolines of the baroclinic term B, (6.8) (blue negative, green positive). The two vector fields, with arrows coloured according to the intensity from red to white, correspond to $\sqrt{8/\rho^2(3-\rho)}\nabla\rho$ and $\sqrt{8/\rho^2(3-\rho)}\nabla\theta$. In the inset, the region of strongest baroclinic production. (b) Vorticity (flood) with superimposed B-isolines and fluid relative velocity with respect to the bubble centre of mass (arrows).

Figure 12(a) shows spatial distribution of B at a particular instant, for the case with $\beta = 58.0$ and $s = 1.2$. It is expressed as the vector product of the two vector fields, $\sqrt{8/\rho^2(3-\rho)}\nabla\rho$ and $\sqrt{8/\rho^2(3-\rho)}\nabla\theta$, shown as arrows in the figure. Apparently, where $|B|$ is large the two local vectors are large (intensity is coloured from red to white) and form a finite angle with each other (see the inset). Elsewhere, either the fields have small intensity, or they are perfectly parallel/antiparallel. By comparing with figure 9, the region of intense baroclinic vorticity production occurs where the compression wave propagating within the bubble interacts with the bubble interface and its intense density gradients ($t/T_c^w = 0.95$, 0.96). Although this may not be the general interpretation (indeed vorticity is generated also assuming the liquid is incompressible), the analysis of our data shows that, in the present specific conditions, the main vorticity production mechanism is associated with the interaction of pressure waves and interfacial density gradients.

Figure 12(b) shows the corresponding vorticity (flood), with the superimposed B-isolines and velocity field in the reference frame translating with the (instantaneous) bubble centre mass velocity. The vorticity generated by the baroclinic term is transported by the fluid velocity and is advected upwards with respect to the translating bubble. The eddying motion associated with the generated vorticity is apparent from the (relative) velocity field. Figure 13 shows different snapshots along the bubble evolution, depicting the same quantities as in figure 12(b). The vorticity survives up to the last frames shown in the figure, despite the considerable diffusion due to viscosity, $1/\rho\nabla \times (1/\rho \nabla \cdot \Sigma)$. This is due to the competing effect of stretching, which tends to intensify the vorticity through the stretching term $(\zeta/\rho) \cdot \nabla u$, related to the increase of the toroid radius since, when approaching the wall, the ring vortex expands radially. As the vortex approaches the wall, secondary vorticity with opposite sign forms right at the wall due to the no-slip condition.

6.4. *Wall pressure*

The pressure waves emitted during collapse propagate with the liquid speed of sound $c = \sqrt{40\theta/(3-\rho)^2 - 6\rho}$ (see Zhao *et al.* 2011) and impact the solid surface as shown
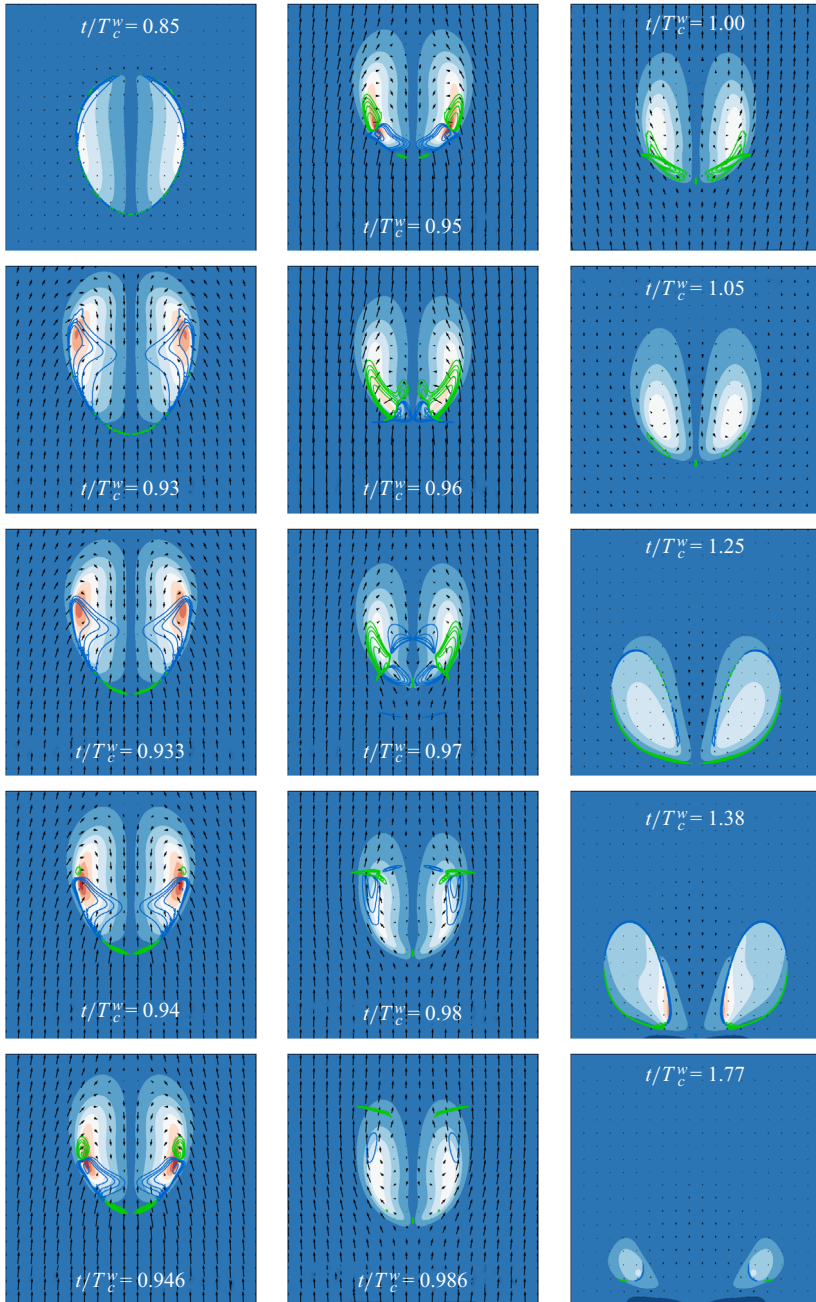
Figure 13. Collapse of a vapour bubble near a solid wall, $\beta = 58.0$, $s = 1.2$, see figure 9. Vorticity (flood), baroclinic vorticity production (solid lines) and relative velocity (vectors), see figure 12(b).

in figure 14, transferring energy to it. The wave front is oriented obliquely with respect to the solid surface, hence its trace generates a disturbance that moves on the wall faster than c, with a velocity v_D that decreases asymptotically to c, as the front becomes normal to the surface, see figure 15 for a qualitative comparison at different β values, where the density gradient intensity increase is apparent for larger β, and figure 16, showing v_D as a function of the radial coordinate. Simple geometric considerations based on the

(*a*) (*b*)
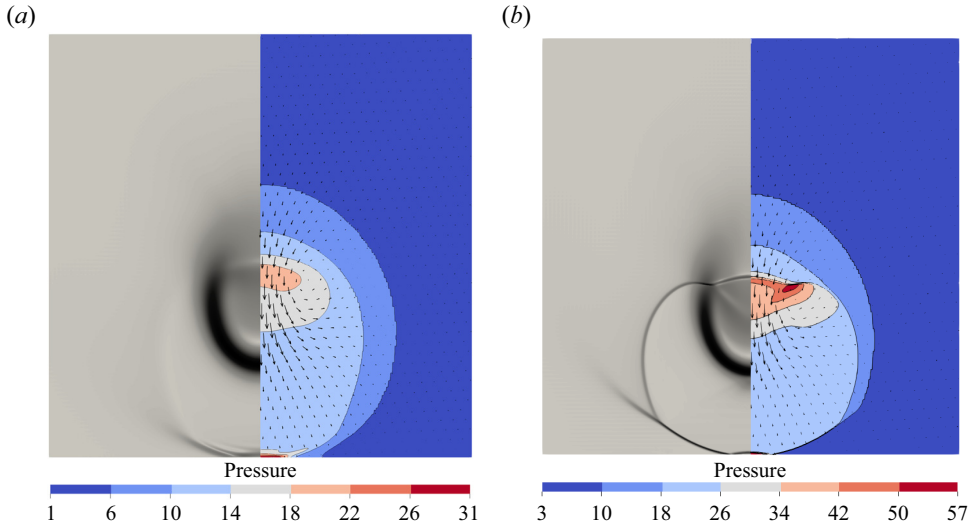
Figure 14. Snapshots of the first time the pressure wave hits the wall: (*a*) $\beta = 28.5$, $s = 1.2$, $t/T_c^w = 1.01$; (*b*) $\beta = 58.0$, $s = 1.2$, $t/T_c^w = 0.98$. Schlieren-like visualisation of the density gradients, dimensionless pressure field (flood, $p_c = 22$ MPa), and absolute velocity vectors.

(*a*) (*b*)
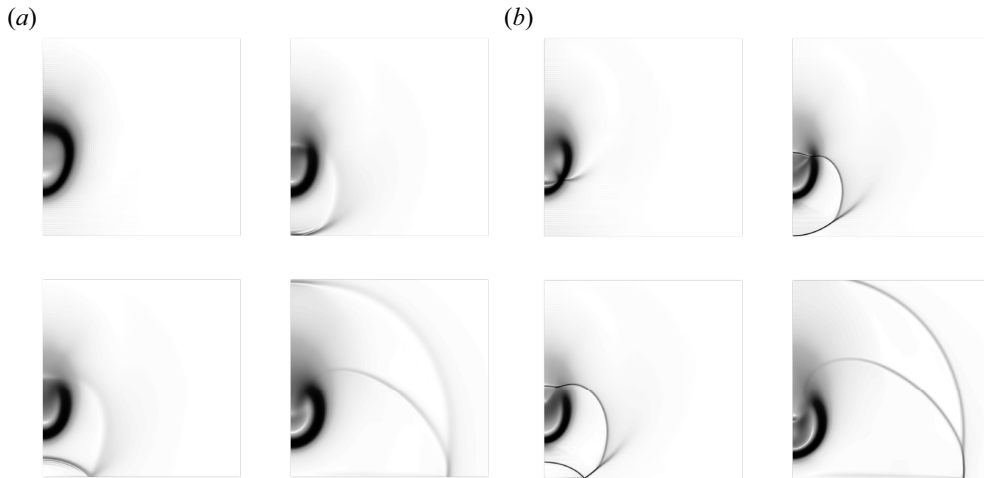
Figure 15. Schlieren-like visualisation of the shock wave travelling in the liquid: (*a*) $\beta = 28.5$, $s = 1.2$ ($t/T_c^w = 0.97$, 1.01, 1.02, 1.06); (*b*) $\beta = 58.0$, $s = 1.2$ ($t/T_c^w = 0.95$, 0.98, 0.99, 1.05).

assumption of spherical propagation lead to $v_D(r) = \sqrt{1 + Z_c^2/r_D^2}$. The load distribution transmitted to the solid is a function of the initial conditions, in terms of overpressure β and relative distance to the wall s, see figure 17, where the wall load envelope is represented for different overpressures (*a*) and distances (*b*). The normal stress

$$T_{zz} = -p_0(\rho, \theta) + \frac{Cn}{2}\left[\left(\frac{\partial \rho}{\partial r}\right)^2 - \left(\frac{\partial \rho}{\partial z}\right)^2\right] + \frac{\rho\, Cn}{r}\left[\frac{\partial}{\partial r}\left(r\frac{\partial \rho}{\partial r}\right) + r\frac{\partial^2 \rho}{\partial z^2}\right]$$

$$- \frac{2}{3Re}\nabla \cdot \boldsymbol{u} + \frac{2}{Re}\frac{\partial u_z}{\partial z}, \tag{6.9}$$
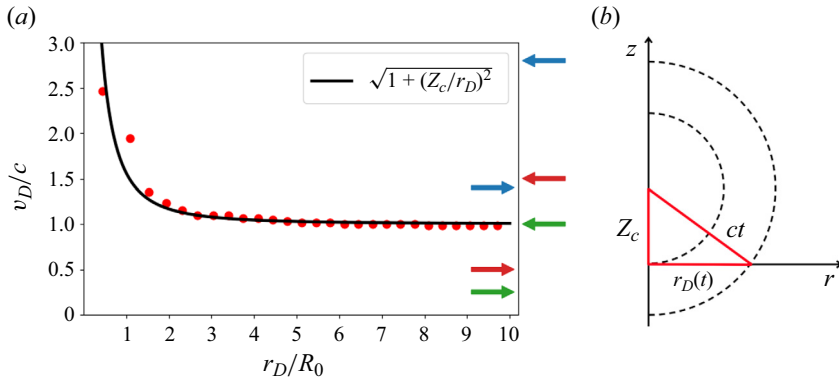
Figure 16. Propagation velocity of the load at the wall as a function of the radial distance from the axis of symmetry ($R_0 = 1$ µm). The velocity at the impact is very high due to the wave front orientation, and progressively converges to the speed of sound in the liquid c. The coloured arrows correspond to the transverse (c_T^*) and longitudinal (c_L^*) wave speeds in the solid for three different scenarios analysed in the simulations.
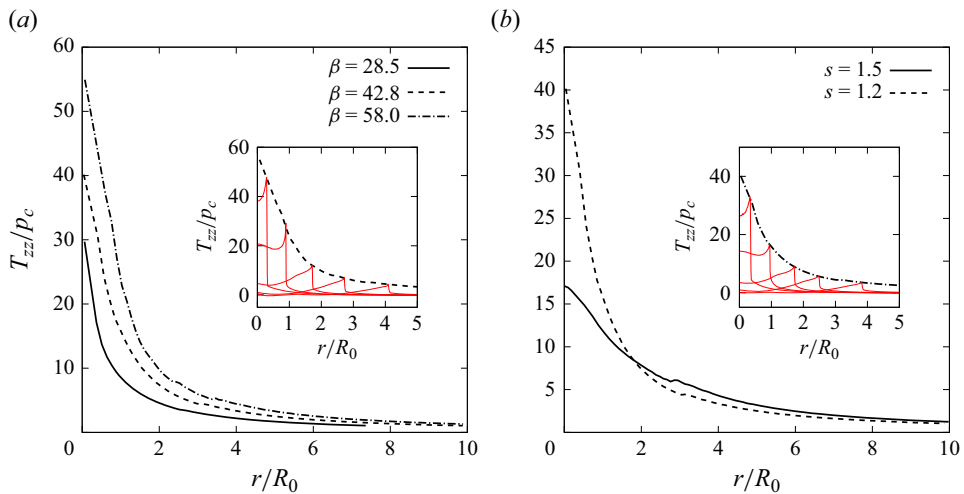

Figure 17. Envelopes of the maximum normal stresses T_{zz} transmitted to the solid surface during loading ($p_c = 22$ MPa, $R_0 = 1$ µm). (*a*) The envelope amplitude is proportional to the overpressure parameter β. In the inset, five different load profiles are shown in red, for $\beta = 58.0$ and $s = 1.2$. (*b*) The shape of the envelopes is influenced by the initial distance of the bubble centre to the solid. As the distance decreases, the impact becomes more concentrated and the maximum pressure increases. In the inset, five different load profiles are shown in red, for $\beta = 42.8$ and $s = 1.2$.

is by far the largest contribution to the stress transmitted to the material ($T_{zz} \gg T_{rz}$) and is responsible for subsequent plastic deformations.

7. Wave propagation in the solid

The solid simulations are performed assuming axisymmetry, with cylindrical coordinates r, θ and z in the domain $\Omega_s = [0, R] \times [0, 2\pi] \times [-H_s, 0]$. The boundary conditions on

999 A72-24

the solid wall $z = 0$ prescribe continuity of stresses

$$\boldsymbol{\sigma}\hat{\boldsymbol{e}}_z = T_{zz}\hat{\boldsymbol{e}}_z, \tag{7.1}$$

where T_{zz} comes from the fluid simulation (6.9). The remaining parts of the domain boundary at $z = -H_s$ and $r = R$ consist of viscous absorbing layers to dampen outward going waves (Hughes 2012). Initially the material is assumed to be completely undeformed and still, $\boldsymbol{r}(\boldsymbol{x}, 0) = \boldsymbol{0}$, $\boldsymbol{v}(\boldsymbol{x}, 0) = \boldsymbol{0}$.

For the moment, we restrict our analysis to a perfectly plastic material, i.e. with $K_H = 0$. In such conditions, the elastic behaviour of the material is fully determined once the two Lamé parameters are prescribed (or, alternatively, one of them plus Poisson's ratio ν), and the plastic behaviour is characterised by the constant yield stress $\sigma_Y(\chi) = \sigma_Y^0$. All the results presented in this section are obtained taking $T_{zz}(r, t)$ data from the fluid simulation with $\beta = 42.8$ and $s = 1.2$.

As stated in § 2, the solid dynamics is assumed not to influence the fluid dynamics, hence the coupling is obtained by just providing the appropriate T_{zz} history to the solid boundary. This assumption is motivated by the high solid/fluid impedance ratio $Z_s/Z_f = \sqrt{2\rho_S\mu_S(1 - \nu)/(1 - 2\nu)}/\rho_l c_l$. A thorough analysis on the effects of the impedance ratio on the bubble dynamics has been recently presented in Cao *et al.* (2021) (see also Brekhovskikh & Godin (2012) for a more general discussion on impedances and waves in layered media) where three different regimes, $Z_s/Z_f \approx 1$, >1 or <1 have been identified. The overall fluid dynamics may change a lot, in particular for what concerns the shock wave reflection, with the results approaching those of the interaction with a rigid wall in the limit $Z_s/Z_f \to \infty$. In the results presented here, we limit our attention to solid materials such that $Z_s/Z_f \geq 10.5$, thus resembling the interaction with a rigid wall, making it unnecessary to fully couple the two systems.

As a consequence of the fluid shock wave impact, elastoplastic waves develop within the material, as introduced in § 4.1. By varying the solid material properties at fixed $T_{zz}(r, t)$ history, three different behaviours of the elastoplastic material are observed and analysed here, corresponding to the arrows in figure 16, which identify the transverse and longitudinal waves speed ($c_T^* < c_L^* < c$ green, $c_T^* < c < c_L^*$ red and $c < c_T^* < c_L^*$ blue). The intermediate red case ($c_T^* = 5.42$, $c_L^* = 10.83$, $\nu = 0.33$), referred here as the transonic case, following the naming convention adopted in solid mechanics, is reported in figure 18 (compare with the sketch in figure 2 for a reference) whose columns include the Von Mises equivalent stress $\sqrt{3/2}|\boldsymbol{\sigma}_{dev}|$, the divergence and the curl of the displacement field, respectively. In the elastic reference solution (first row of figure 18) the whole complex system of waves outlined in § 4.1 is apparent in the first column. The hemispherical wavefronts located at $r \approx 8$ and $r \approx 4$ enclose longitudinal and transversal waves, respectively, that are decoupled and individually represented in the second and third columns in the form of the divergence and curl fields. The fluid disturbance, located at $r \approx 6$, generates the transonic elastic conical wave that connects to the transverse wavefront, first column. The head or Von Schmidt conical wavefront, of weaker intensity, generated at the solid boundary in correspondence with the longitudinal wavefront, is noticeable in the first column. Finally, the Rayleigh waves are visible in the narrow zone located under the solid surface at $r \approx 4$, in columns 2 and 3. The plastic solutions, second and third rows of figure 18, $\sigma_Y^0 = 1 \times 10^{-2}$ and 5×10^{-3}, respectively, appear to be similar to the elastic solution in the wave propagation, but different in a subsuperficial zone below the bubble ($R_0 = 1$), where the stress intensity is higher and the divergence and curl fields are non-negligible, meaning that some non-elastic mechanism is at play. By comparing the intensities in the three figures it is clear how, in the plastic materials, some of the
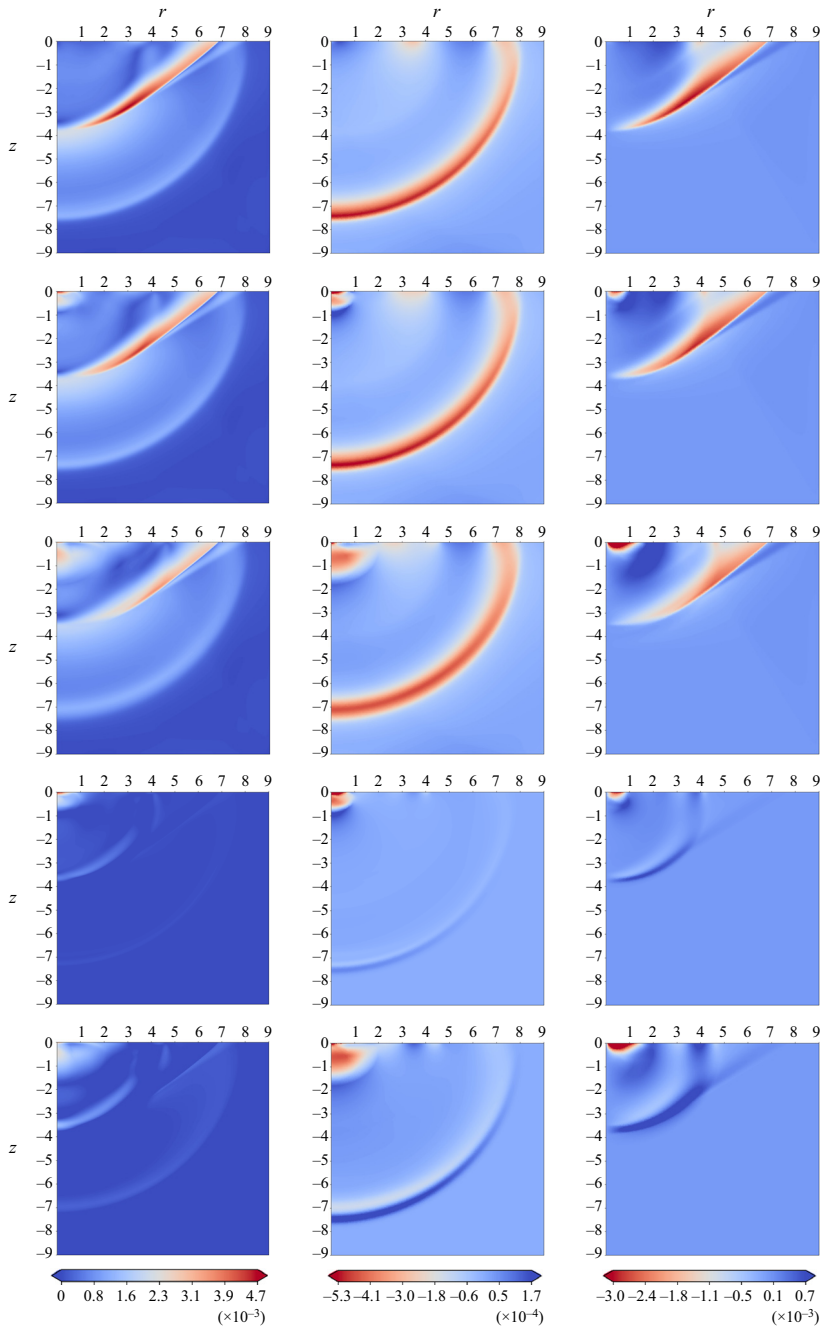
Figure 18. Von Mises stress, divergence and curl of the displacement field organised by columns, at dimensionless time $t/T_c^W = 1.39$ (unit length corresponding to 1 µm). Cases organised by rows: (1) elastic case, (2) plastic case with $\sigma_Y^0 = 1 \times 10^{-2}$, (3) plastic case with $\sigma_Y^0 = 5 \times 10^{-3}$, (4) row 2–row 1 and (5) row 3–row 1. The nonlinearity of the dynamic elastoplastic problem affects not only the subsuperficial area corresponding to the bubble position, but also the propagation of the elastic wave front.
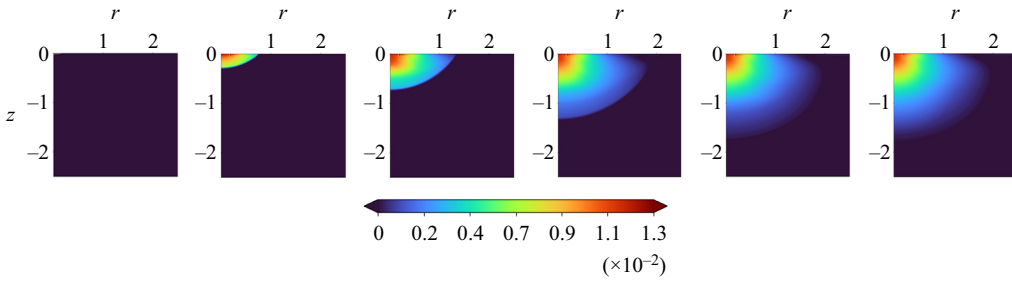
Figure 19. Plastic strain norm $|\boldsymbol{\epsilon}_p|$ propagation in time for the transonic plastic case with $\sigma_Y^0 = 5 \times 10^{-3}$. The elastoplastic wave propagating in the solid is apparent. From left to right, dimensionless times $t/T_c^w = 0.99$, 1.01, 1.04, 1.08, 1.10 and 1.61.

energy transmitted to the solid is dissipated by permanently deforming the narrow zone below the bubble, thus resulting in weaker energies transported by the elastic waves. The difference between the elastic and the corresponding plastic solutions is presented in the third and fourth rows. This visualisation highlights how not only the subsuperficial zone below the bubble is influenced by plasticity, but also the propagation of the elastic waves, whose wavefront is less pronounced. This effect is also more evident in the second plastic case, with a smaller yield stress σ_Y^0, thus attaining larger plastic deformations. This fact was already introduced in § 4.1, where the nonlinearity of the problem was discussed and the possibility of a permanent plastic deformation having an influence on the underlying elastic dynamics was assessed.

The resulting plastic deformation, that evolves according to (4.3), is shown in the sequence of figure 19 for the case with $\sigma_Y^0 = 5 \times 10^{-3}$ (similar results are obtained for $\sigma_Y^0 = 1 \times 10^{-2}$). The hemispherical front of plastic deformation clearly expands during time, up until a point where the energy transmitted by the fluid shock wave is below the distortional energy needed to plastically deform the material. As a result, a finite region is permanently deformed in those places where the stresses were maximal.

A different qualitative picture can be obtained by varying c_L and c_T in such a way that the wave propagation on the solid surface is completely supersonic or subsonic with respect to the wave speeds in the solid, green and blue arrows in figure 16, respectively. In the former case, figure 20 (see panel *a* for the elastic reference solution), since $c > c_L$, a new conical wavefront emerges, originating at the solid–liquid interface in correspondence with the moving load ($r \approx 8$) and connecting to the hemispherical wavefront of the longitudinal waves ($r = z \approx 3.5$). In these conditions, the Von Schmidt wavefront and the Rayleigh waves are invisible. Looking at the elastoplastic solutions in figure 20(*b–d*), ordered for decreasing σ_Y^0, it should be noted how the maximum attained stress in the material obviously decreases and the wavefronts become progressively more diffused, and interact with each other giving rise to different structures. Significant differences are also found in the subsuperficial region below the bubble, where the material is permanently deformed. The resulting plastic deformation is shown in figure 21 for the same three cases ordered by decreasing σ_Y^0, where it is clearly visible how the region interested by plasticity spreads and attains larger deformations for decreasing σ_Y^0.

Finally, the subsonic case (blue arrows in figure 16) is shown in figure 22, where the Von Mises stress for the purely elastic (*a*) and the plastic (*b*) cases is reported. The main difference with previous cases is the absence of conical wavefronts induced by the fluid disturbance, the only one being the already mentioned Von Schmidt conical wavefront generated at the solid–fluid interface. The only discrepancy between the elastic
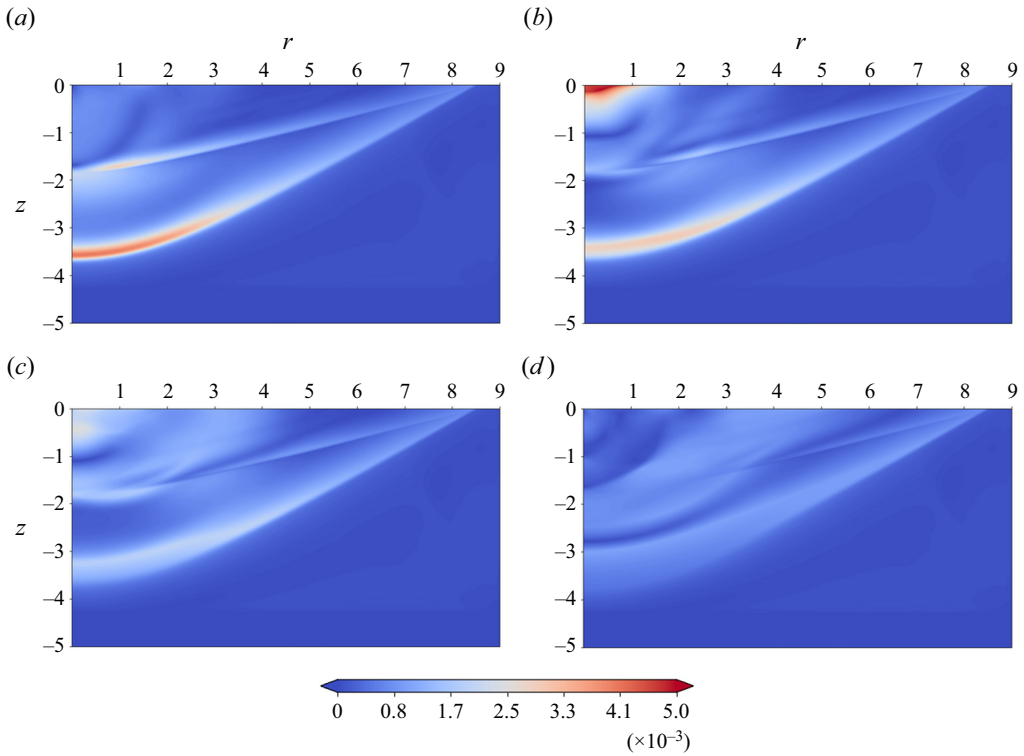
Figure 20. Von Mises stress at $t/T_c^w = 1.50$ for the supersonic case and for three different yield stresses: (a) elastic, (b) plastic, $\sigma_Y^0 = 5 \times 10^{-3}$, (c) $\sigma_Y^0 = 2.5 \times 10^{-3}$ and (d) $\sigma_Y^0 = 1 \times 10^{-3}$.

and plastic solutions is in the region enclosed by the transversal wavefront ($r < 3$), where the disturbance excites the solid material. Comparing this case with the previous cases, it is interesting to note how the plastically deformed region is particularly significant and spreads more in the radial direction. This is a direct effect of the load being applied, over time, in roughly the same region where the transversal and Rayleigh waves are located.

7.1. Plastic dissipation in the solid

The dissipation in the solid material due to plasticity can be evaluated using the relation $\mathcal{D}(r, z, t) = \sqrt{2/3}\sigma_Y^0|\dot{\epsilon}_p(r, z, t)|$, which, by recalling that $\alpha_p(t) = \sqrt{2/3}\int_0^t |\dot{\epsilon}_p(r, z, \tau)|\,d\tau$, can be integrated over time and space to obtain the energy dissipated as permanent plastic deformation in the material,

$$E_{\mathcal{D}} = \int_0^t \int_V \mathcal{D}(r, z, \tau)\,dV\,d\tau = \sigma_Y^0 \int_V \alpha_p(r, z, t)2\pi r\,dr\,dz. \tag{7.2}$$

On the other hand, the energy transferred to the solid by the fluid load on the wall is

$$E_{wall} = \int_0^t \mathcal{P}_{wall}(\tau)\,d\tau = \int_0^t \int_0^R T_{zz}(r, 0)\boldsymbol{v}(r, 0)2\pi r\,dr\,d\tau. \tag{7.3}$$
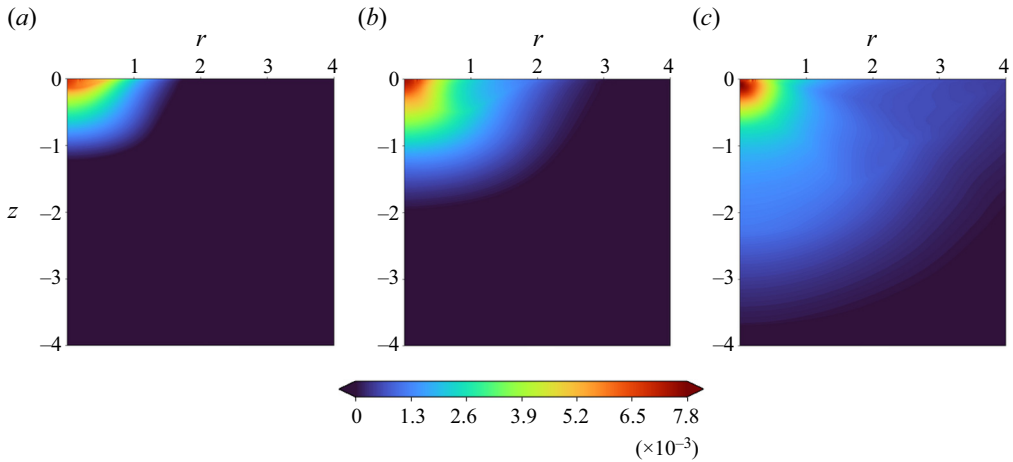
999 A72-28

Figure 21. Permanent plastic deformation norm $|\epsilon_p|$ for the supersonic case in figure 20: (a) $\sigma_Y^0 = 5 \times 10^{-3}$, (b) $\sigma_Y^0 = 2.5 \times 10^{-3}$ and (c) $\sigma_Y^0 = 1 \times 10^{-3}$.
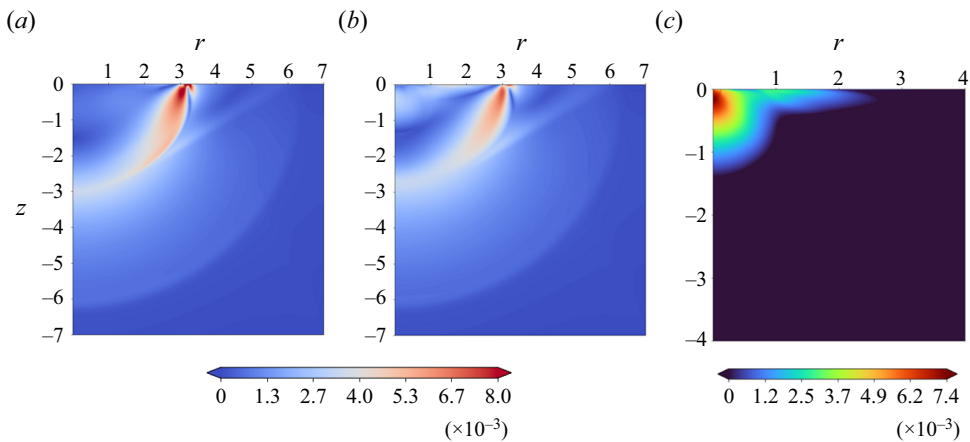

Figure 22. Von Mises stress for the subsonic case at $t/T_c^w = 1.13$: (a) elastic and (b) plastic with $\sigma_Y^0 = 8 \times 10^{-3}$. The load excites the solid roughly at the Rayleigh wave location over time, thus resulting in a permanent plastic deformation norm $|\epsilon_p|$ that spreads also radially, as shown in panel (c).

The evolution of the power and energy transmitted to the wall, and the percentage of energy that is dissipated in plastic deformation are shown in figure 23 for five different plastic cases. As expected, at fixed elastic parameters, the materials with lower σ_Y^0 dissipate more.

8. Conclusions and perspectives

The collapse of a vapour microbubble over an elastoplastic solid wall, caused by an external high-pressure liquid, has been investigated by adopting a diffuse interface model for the fluid and a dynamic elastoplastic model for the solid. At the same time, inertial effects, typical of the macroscale, remain crucial at these scales. In particular, jet formation and topological transitions are observed for microbubble collapse triggered by an initial overpressure in the liquid. A complex system of shock waves, emerging from the bubble interior during collapse, is reflected and refracted at the bubble interface, and then
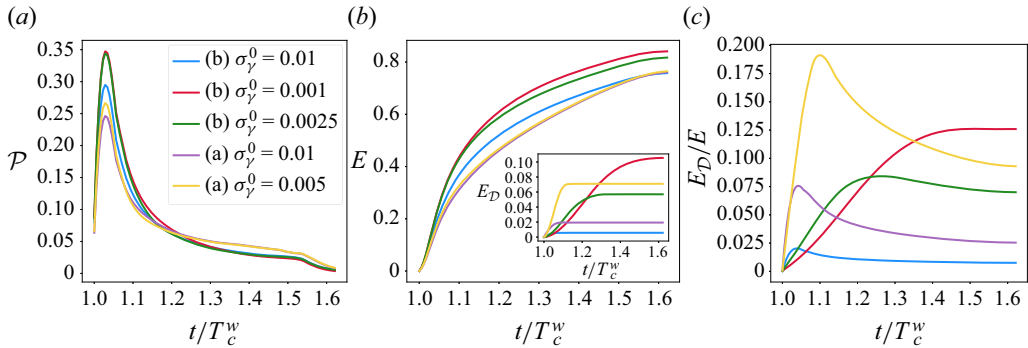
999 A72-29

Figure 23. (*a*–*c*) Power transmitted to the solid wall, energy transmitted to the solid wall (with total energy dissipated in plastic deformation in the inset) and percentage of energy dissipated in plastic deformation vs dimensionless time, for five different plastic materials. The time scale is shifted by T_c^w to start at collapse time. The two cases labelled with (a) are for the transonic case (red arrows in figure 16), whereas (b) refers to three supersonic cases (green arrows in figure 16).

propagates in the liquid to later impact the solid wall and transfer energy to it. We have shown that the interaction of the fluid shock wave with the bubble interface produces baroclinic vorticity, inducing the typical circulatory motion associated with microjetting.

The fluid stress on the elastoplastic wall transfers energy to the solid. Part of this energy is transported outwards by elastic waves, part is dissipated by plasticity in the permanent deformation of the material. The radiated waves consist of longitudinal, transversal, Rayleigh and conical head waves. In the meanwhile, plastic deformation occurs in the form of expanding plasticity waves. The permanent deformation of the solid accumulates in a subsuperficial region below the bubble, which extends to at least half of the initial bubble volume in the solid. The two wave components are coupled and, depending on conditions, elastic propagation can be influenced by the plastic deformation. It is found that the permanent deformation is particularly significant in the case of a disturbance moving close to the velocity of Rayleigh and transverse (shear) waves ($v_D \simeq c_R \simeq c_T$). This sounds natural after noting that the adopted plasticity criterion (Von Mises) neglects volumetric deformations and plasticity occurs when distortional (shear) energy exceeds the critical thresholds.

Throughout the paper, we assumed axisymmetry of the collapse and elastoplastic wave propagation. Reuter, Deiter & Ohl (2022) recently showed that the non-axisymmetric self-focusing mechanism may contribute significantly to erosion for single-bubble cavitation, in particular in extreme vicinity of metallic surfaces. These recent experimental findings call for three-dimensional non-axisymmetric simulations, which, given the significant computational demand, are reserved for future work, together with the possible extension to real fluids (Benilov 2020; Magaletti *et al.* 2021) and to binary mixtures (Liu, Amberg & Do-Quang 2016; Mukherjee & Gomez 2022; Benilov 2023).

As a final comment concerning the plasticity model, we focused here on perfectly plastic materials with hardening modulus $K_H = 0$. Hardening, $K_H > 0$, would only affect the behaviour in the plastic regime, requiring an increasingly larger threshold to be exceeded to plastically deform the material, without changing the overall qualitative picture. The model can be further extended to account for rate-dependency and damage effects, also generalising the yield criterion to describe non-metal (e.g. soft) materials.

Supplementary material. Supplementary material is available at https://doi.org/10.1017/jfm.2024.925.

999 A72-30

Author ORCIDs.

Dario Abbondanza https://orcid.org/0000-0001-8303-1993;

Mirko Gallo https://orcid.org/0000-0003-3395-2246;

Carlo Massimo Casciola https://orcid.org/0000-0001-8795-4517.

Appendix A. Elastoplasticity modelling

The purpose of the present appendix is to briefly recapitulate basic notions of continuum mechanics and plasticity theory and introduce the plasticity model used in the simulations. Mainly, this appendix is added to the main text for the convenience of readers not acquainted with this class of theories. Most of the material is classical and can be found in the specialised literature, even though a few elements of novelty may be found in our attempt to provide a concise, but self-contained treatment. A review of nonlinear plasticity theory may be found, for example, in Antman & Szymczak (1989) and Antman (2005), whereas the linearised model we actually employ and rederive from the nonlinear theory is described in Lubliner (2008). The formulation we use belongs to the class of rate-independent, isothermal plasticity models with isotropic hardening, even though it can be readily extended in several respects, e.g. by considering thermal effects and including rate-dependency.

A.1. *Plasticity model*

The configuration of a body is defined in terms of the map from the reference configuration (Lagrangian variables) to the current one, $x = \chi(X, t) = X + r(X, t)$ (Eulerian variables), where r is the displacement. The deformation gradient $F = \partial x / \partial X$ and the (nonlinear) strain $E = (F^T \cdot F - I)/2$ are central elements of the theory (Gurtin 1982). Classically, momentum conservation in Lagrangian variables reads

$$\rho_0 \ddot{r} = \nabla_X \cdot (F \cdot S) + \rho_0 f_0, \tag{A1}$$

where ρ_0 is the (possibly space-dependent) constant-in-time mass density in the Lagrangian description, f_0 is the body force per unit mass and the (symmetric) second Piola–Kirchhoff stress tensor is $S = J F^{-1} \Sigma_S F^{-T}$, with Σ_S the solid's Cauchy stress, $J = |F|$ the Jacobian determinant and the superscripts T and -1 denote matrix transposition and inversion, respectively (Gurtin *et al.* 2010).

It is well known that, when the elastoplastic solid undergoes deformation, the displacement cannot be split into elastic and plastic components. However, the deformation gradient can always be multiplicatively decomposed as the product of elastic and plastic parts, $F = F_e \cdot F_p$, allowing the introduction of the plastic strain $E_p = (F_p^T \cdot F_p - I)/2$ (Lubliner 2008).

We assume the plastic strain and an additional scalar object, α_p, as internal variables defining the plastic state. The Helmholtz free energy (per unit reference volume) in a (locally) relaxed state where $F_e = 0$ is taken to depend on the internal variable α_p, such that, under loading, it takes the form $\hat{f} = \hat{f}(E - E_p; \alpha_p)$, providing the stress tensor as

$S = \partial \hat{f}(E - E_p; \alpha_p)/\partial E$. In the unloaded material, $S = 0$ and the stress should, in general, behave linearly in the strain difference when $E \simeq E_p$,

$$\hat{f} = \hat{f}_0(\alpha_p) + \tfrac{1}{2}(E - E_p) : C_e(\alpha_p) : (E - E_p) + O(|E - E_p|^3), \tag{A2}$$

where the (fourth-order) elastic tensor is $C_e(\alpha_p)$.

The Clausius–Duhem inequality, $S : \dot{E} - \dot{\hat{f}} \geq 0$, expresses the second principle of thermodynamics and defines the positive-definite dissipation function (Gurtin *et al.* 2010)

$$\mathcal{D} = S : \dot{E}_p + \chi \dot{\alpha}_p \geq 0, \tag{A3}$$

where the hardening variable $\chi = -\partial \hat{f}/\partial \alpha_p$ is conjugate to α_p. For the model used in the simulations, the physical interpretation of both variables will become clear at the end of the next appendix, where the formulation is specified in every detail.

A crucial ingredient in plasticity theory is the yield function, expressed here in terms of S and χ, that defines the admissible states by the inequality

$$\Phi = \Phi(S, \chi) \leq 0. \tag{A4}$$

Material plasticisation occurs only on the yield surface during plastic loading, i.e. for $\Phi = 0$ and $\partial \Phi/\partial S : \dot{S} > 0$, requiring the state to remain on the yield surface, $\dot{\Phi} = \dot{S} : \partial \Phi/\partial S + \dot{\chi} \partial \Phi/\partial \chi = 0$ (Lubliner 2008).

We shall assume a maximum dissipation principle (Mises 1928; Taylor 1947; Simo & Hughes 2006), namely the stress S and the dual internal variable χ to be realised should maximise the dissipation (A3) for given $\dot{E}_p$ and $\dot{\alpha}_p$ given the constraint (A4),

$$\dot{E}_p = \frac{\partial \mathcal{D}}{\partial S} = \gamma \frac{\partial \Phi}{\partial S}, \quad \dot{\alpha}_p = \frac{\partial \mathcal{D}}{\partial \chi} = \gamma \frac{\partial \Phi}{\partial \chi}, \tag{A5a,b}$$

where γ is the (Lagrange) plastic multiplier different from zero only during plastic loading. The equations of E_p and α_p are then completely defined after γ is evaluated explicitly by requiring the state to remain on the yield surface under plastic loading. Taking $\dot{S}$ and $\dot{\chi}$ from their definitions in terms of free energy and substituting into the equation $\dot{\Phi} = 0$, a bit of algebra leads to the cumbersome but eventually simple expression

$$\gamma = \dot{E} : \left[\frac{\partial}{\partial E}\left(\frac{\partial \hat{f}}{\partial E} \right) : \frac{\partial \Phi}{\partial S} - \frac{\partial}{\partial E}\left(\frac{\partial \hat{f}}{\partial \alpha_p} \right) \frac{\partial \Phi}{\partial \chi} \right] \frac{1}{D}, \tag{A6}$$

where the denominator is

$$D = \left[\frac{\partial \Phi}{\partial S} : \frac{\partial}{\partial E}\left(\frac{\partial \hat{f}}{\partial E} \right) - \frac{\partial \Phi}{\partial \chi} \frac{\partial}{\partial \alpha_p}\left(\frac{\partial \hat{f}}{\partial E} \right) \right] : \frac{\partial \Phi}{\partial S}$$

$$+ \left[-\frac{\partial \Phi}{\partial S} : \frac{\partial}{\partial E}\left(\frac{\partial \hat{f}}{\partial \alpha_p} \right) + \frac{\partial \Phi}{\partial \chi} \frac{\partial}{\partial \alpha_p}\left(\frac{\partial \hat{f}}{\partial \alpha_p} \right) \right] \frac{\partial \Phi}{\partial \chi}. \tag{A7}$$

Substitution into (A5) yields

$$\dot{E}_p = M_{E_p} : \dot{E}, \quad \dot{\alpha}_p = M_{\alpha_p} : \dot{E} \tag{A8a,b}$$

for suitable tensors M_{E_p} and M_{α_p} whose explicit form is easily evaluated. Concerning stress, from its definition as the partial derivative of the free energy with respect to the

999 A72-32

strain, its time derivative is readily arranged as

$$\dot{S} = \left[\frac{\partial}{\partial E} \left(\frac{\partial \hat{f}}{\partial E} \right) - M_S \right] : \dot{E}, \tag{A9}$$

where the explicit expression of M_S is straightforwardly worked out using the second equation in (A8).

A.2. *Linearisation of the plasticity model*

The above model can be readily linearised under the assumption of small elastoplastic displacements, $|r| = O(\epsilon)$ together with its derivatives. It readily follows that $r(X, t) = r(x, t) + O(\epsilon^2)$, $\ddot{r}(X, t) = \partial^2 r(x, t)/\partial t^2 + O(\epsilon^2)$ and $E(X, t) = \epsilon(x, t) + O(\epsilon^2)$, with $\epsilon = (\nabla_x r + \nabla_x r^T)/2$ the infinitesimal strain.

From the assumption of small displacements, one also finds $|G_p| = |G_e| = O(\epsilon)$, where $G_{p/e} = I - F_{p/e}$, which immediately leads to the additive decomposition of the (infinitesimal) strain in terms of plastic and elastic contributions, $\epsilon = \epsilon_p + \epsilon_e$ where $\epsilon_{p/e} = (G_{p/e} + G_{p/e}^T)/2$.

Concerning mass, one readily finds $\rho(x, t) = \rho_0(x) + O(\epsilon)$, whereas momentum conservation eventually becomes

$$\rho_0 \frac{\partial^2 r}{\partial t^2} = \nabla_x \cdot \sigma + \rho_0 f, \tag{A10}$$

once the asymptotic identity of Cauchy and second Piola–Kirchhoff stresses, $\sigma = \Sigma_S + O(\epsilon^2) = S + O(\epsilon^2)$, is realised.

The Helmholtz free energy, in its quadratic approximation for small strains (A2), reads

$$\hat{f} = \hat{f}_0(\alpha_p) + \tfrac{1}{2}(\epsilon - \epsilon_p) : C_e(\alpha_p) : (\epsilon - \epsilon_p) + O(\epsilon^3), \tag{A11}$$

where the fourth-order elastic tensor C_e, the second derivative of the free energy with respect to strain, expresses the stress as $\sigma = C_e(\alpha_p) : \epsilon_e + O(\epsilon^2)$. For future reference, we note that $\partial/\partial\alpha_p(\partial\hat{f}/\partial E) = O(\epsilon)$. In the simulations described in the main text, $\hat{f}_0(\alpha_p) = 1/2K_H\alpha_p^2$ where K_H is the hardening modulus and the elastic tensor takes the usual isotropic form in terms of the two sole Lamé coefficients, the shear modulus $\mu_S(\alpha_p)$ and $\lambda_S(\alpha_p) = K - 2/3\mu_S$ where $K(\alpha_p)$ is the bulk modulus, respectively (Gurtin 1982).

To completely define the model, the yield function needs being specified, and is here taken to be of the Von Mises form (Mises 1913),

$$\Phi(\sigma, \chi) = f_{dev}^e(\sigma) - f_{dev}^c[\sigma_Y(\chi)]. \tag{A12}$$

Here $f_{dev}^e = \sigma_{dev} : \sigma_{dev}/(4\mu_S)$ is the distortional contribution to the elastic free energy, with $\sigma_{dev} = \sigma - 1/3\,\mathrm{tr}(\sigma)I$ the deviatoric stress. We use $f_{dev}^c = [\sigma_Y(\chi)]^2/(6\mu_S)$ to denote its critical value after which the material yields. Finally, $\sigma_Y(\chi) = \sigma_Y^0 - \chi$ is the (state-dependent, uniaxial) yield stress with value $\sigma_Y(0) = \sigma_Y^0$ before plasticisation where $\chi = 0$. In other words, the hardening variable is physically identified with (minus) the difference of current and pristine yield stress, $-\chi = \sigma_Y - \sigma_Y^0 > 0$.

The tensors in (A8) are identically zero unless the material is under plastic loading. On the other hand, since, based on the yield function (A12) $\partial\Phi/\partial\sigma = \sigma_{dev}/(2\mu_S)$,

$\partial\Phi/\partial\chi = \sigma_Y/(3\mu_S)$, their explicit, linearised expressions under plastic loading, to accuracy $O(\epsilon)$, read

$$M_{E_p}^{Lin} = \frac{\partial\Phi}{\partial\boldsymbol{\sigma}} : C_e(\alpha_p) \otimes \frac{\partial\Phi}{\partial\boldsymbol{\sigma}}\frac{1}{D^{Lin}} = \frac{\boldsymbol{\sigma}_{dev} : C_e(\alpha_p) \otimes \boldsymbol{\sigma}_{dev}}{4\mu_S^2 D^{Lin}}, \tag{A13a}$$

$$M_{\alpha_p}^{Lin} = C_e(\alpha_p) : \frac{\partial\Phi}{\partial\boldsymbol{\sigma}}\frac{\partial\Phi}{\partial\chi}\frac{1}{D^{Lin}} = \frac{\sigma_Y C_e(\alpha_p) : \boldsymbol{\sigma}_{dev}}{6\mu_S^2 D^{Lin}}, \tag{A13b}$$

where $D^{Lin} = \partial\Phi/\partial\boldsymbol{\sigma} : C_e(\alpha_p) : \partial\Phi/\partial\boldsymbol{\sigma} + \partial\Phi/\partial\chi\hat{f}_0''\partial\Phi/\partial\chi$, leading to the evolution equations

$$\dot{\boldsymbol{\epsilon}}_p = M_{E_p}^{Lin} : \dot{\boldsymbol{\epsilon}}, \quad \dot{\alpha}_p = M_{\alpha_p}^{Lin} : \dot{\boldsymbol{\epsilon}}. \tag{A14a,b}$$

Finally, (A9), the linearised stress evolution equation under plastic loading, is

$$M_S^{Lin} = \left[C_e(\alpha_p) : \frac{\partial\Phi}{\partial\boldsymbol{\sigma}} \right] \otimes \left[\frac{\partial\Phi}{\partial\boldsymbol{\sigma}} : C_e(\alpha_p)\frac{1}{D^{Lin}} \right], \tag{A15}$$

where $\otimes$ is the tensor product of the two tensors within square brackets.

From (A14), it is an easy, though laborious, matter to identify the physical meaning of the internal variable α_p as (proportional to) the accumulated plastic strain $\alpha_p(t) = \sqrt{2/3}\int_0^t |\dot{\epsilon}_p|\,\mathrm{d}t$ and to recast its evolution equation into an equivalent form for the yield stress, after exploiting the chain of identities $\dot{\sigma}_Y = -\dot{\chi} = K_H\dot{\alpha}_p$. Moreover, the condition for plastic loading is readily found equivalent to $|\boldsymbol{\sigma}_{dev}| = \sqrt{2/3}\sigma_Y$ together with $\boldsymbol{\sigma}_{dev} : \dot{\boldsymbol{\epsilon}} > 0$.

Using the explicit form of the derivatives $\partial\Phi/\partial\boldsymbol{\sigma}$, $\partial\Phi/\partial\chi$ and realising that $\partial\Phi/\partial\boldsymbol{\sigma} : C_e(\alpha_p) = \boldsymbol{\sigma}_{dev}$ one eventually obtains the model compendium given in the main text (see §4).

Appendix B. The sharp limit of the diffuse interface equations

The purpose of the present appendix is to show how the traditional equations of the sharp interface model are exactly recovered from the present diffuse interface description. The starting point is the diffuse interface form of the momentum equation

$$\frac{\partial\rho\boldsymbol{u}}{\partial t} + \nabla \cdot (\rho\boldsymbol{u} \otimes \boldsymbol{u}) = \nabla \cdot (\boldsymbol{T}_{rev} + \boldsymbol{\Sigma}), \tag{B1}$$

with the reversible component of the stress tensor given by

$$\boldsymbol{T}_{rev} = -\left(p_0 - \frac{\lambda}{2}|\nabla\rho|^2 - \rho\nabla \cdot (\lambda\nabla\rho) \right)\boldsymbol{I} - \lambda\nabla\rho \otimes \nabla\rho, \tag{B2}$$

and

$$\boldsymbol{\Sigma} = \eta(\nabla\boldsymbol{u} + (\nabla\boldsymbol{u})^{\mathrm{T}}) - \tilde{\eta}(\nabla \cdot \boldsymbol{u})\boldsymbol{I} \tag{B3}$$

the standard Newtonian part. The divergence of the reversible part of the stress tensor can be rearranged as

$$\nabla \cdot \boldsymbol{T}_{rev} = -\nabla\hat{p} + \nabla \cdot K, \tag{B4}$$

with a suitably modified pressure $\hat{p} = p_0 + \lambda/2|\nabla\rho|^2 - \rho\nabla \cdot (\lambda\nabla\rho)$ and a symmetric second-order tensor $K = \lambda|\nabla\rho|^2\boldsymbol{I} - \lambda\nabla\rho \otimes \nabla\rho$.

In the diffuse interface model, the interfacial layer has a small, but finite thickness ℓ_{lv}, (3.4). To recover the sharp interface description we have to assume that the ratio of interface thickness and external scale $\epsilon = \ell_{lv}/R_0$ tends to zero. In the following, spatial distances are made dimensionless with the outer scale R_0 such that the interfacial layer more or less extends in the range $-\epsilon/2 \le n \le \epsilon/2$.

We describe a neighbourhood of the interface using a local system of curvilinear coordinates, with n the coordinate in the normal direction and $\xi^{1/2}$ tangential coordinates, such that $\boldsymbol{r} = \boldsymbol{g}_\alpha \xi^\alpha + n\boldsymbol{n} = \boldsymbol{r}_\pi + n\boldsymbol{n}$, $\boldsymbol{\nabla} = \boldsymbol{g}^\alpha \partial/\partial \xi^\alpha + \boldsymbol{n}\partial/\partial n = \nabla_\pi + \boldsymbol{n}\,\partial/\partial n$, with $\boldsymbol{g}_\alpha = \partial \boldsymbol{r}/\partial \xi^\alpha$ the covariant base vectors ($\alpha = 1, 2$) and $\boldsymbol{g}^\beta$ the corresponding contravariant base elements on the tangent plane.

The inner region of the field, corresponding to the interfacial layer, is better described using the inner variable $\nu = n/\epsilon$, such that, in the spirit of matched asymptotic expansion, $-\infty \le \nu \le \infty$. The gradient operator reads $\boldsymbol{\nabla} = \boldsymbol{n}/\epsilon\,\partial/\partial \nu + \nabla_\pi$ in the inner variable, e.g.

$$\boldsymbol{\nabla}\rho = \boldsymbol{n}\frac{1}{\epsilon}\frac{\partial \rho}{\partial \nu} + \nabla_\pi \rho, \tag{B5}$$

$$\boldsymbol{K} = \frac{\lambda}{\epsilon}\left(\frac{1}{\epsilon}\left(\frac{\partial \rho}{\partial \nu}\right)^2 (\boldsymbol{I} - \boldsymbol{n} \otimes \boldsymbol{n}) + \frac{\partial \rho}{\partial \nu}(\boldsymbol{n} \otimes \nabla_\pi \rho + \nabla_\pi \rho \otimes \boldsymbol{n}) + \epsilon(|\nabla_\pi \rho|^2 \boldsymbol{I} - \nabla_\pi \rho \otimes \nabla_\pi \rho)\right), \tag{B6}$$

$$\hat{p} = p_0 + \frac{\lambda}{2\epsilon}\left(\frac{1}{\epsilon}\left(\frac{\partial \rho}{\partial \nu}\right)^2 + \epsilon|\nabla_\pi \rho|^2\right) - \frac{\lambda}{\epsilon}\rho\left(\frac{1}{\epsilon}\frac{\partial^2 \rho}{\partial \nu^2} + \frac{\partial \rho}{\partial \nu}\nabla_\pi \cdot \boldsymbol{n} + \epsilon\nabla_\pi^2 \rho\right). \tag{B7}$$

The surface tension (3.5) reads

$$\sigma = \int_{-\infty}^{+\infty} \lambda\left(\frac{\partial \rho}{\partial n}\right)^2 \mathrm{d}n = \frac{\lambda}{\epsilon}\int_{-\infty}^{+\infty}\left(\frac{\partial \rho}{\partial \nu}\right)^2 \mathrm{d}\nu, \tag{B8}$$

which shows that, in the limit of vanishing interfacial thickness, the ratio $\gamma = \lambda/\epsilon$ and the integral $\int (\partial \rho/\partial \nu)^2 \, \mathrm{d}\nu$ both remain finite and positive.

In the sharp interface limit, the forces exchanged across the two sides of the interface appear as concentrated effects, with intensity given by the integral across the interfacial layer of $\boldsymbol{\nabla} \cdot \boldsymbol{T}_{rev}$. Straightforward calculations show that

$$\boldsymbol{\nabla} \cdot \boldsymbol{K} = \boldsymbol{n} \cdot \frac{1}{\epsilon}\gamma\frac{\partial}{\partial \nu}\left(\frac{1}{\epsilon}\left(\frac{\partial \rho}{\partial \nu}\right)^2 (\boldsymbol{I} - \boldsymbol{n} \otimes \boldsymbol{n}) + \frac{\partial \rho}{\partial \nu}(\boldsymbol{n} \otimes \nabla_\pi \rho + \nabla_\pi \rho \otimes \boldsymbol{n})\right.$$
$$+ \epsilon(|\nabla_\pi \rho|^2 \boldsymbol{I} + \nabla_\pi \rho \otimes \nabla_\pi \rho)\Big) + \nabla_\pi \cdot \gamma\left(\frac{1}{\epsilon}\left(\frac{\partial \rho}{\partial \nu}\right)^2 (\boldsymbol{I} - \boldsymbol{n} \otimes \boldsymbol{n})\right.$$
$$+ \frac{\partial \rho}{\partial \nu}(\boldsymbol{n} \otimes \nabla_\pi \rho + \nabla_\pi \rho \otimes \boldsymbol{n}) + \epsilon(|\nabla_\pi \rho|^2 \boldsymbol{I} + \nabla_\pi \rho \otimes \nabla_\pi \rho)\Big), \tag{B9}$$

that is,

$$\boldsymbol{\nabla} \cdot \boldsymbol{K} = \frac{\gamma}{\epsilon}\boldsymbol{n} \cdot \frac{\partial}{\partial \nu}\left(\frac{\partial \rho}{\partial \nu}(\boldsymbol{n} \otimes \nabla_\pi \rho + \nabla_\pi \rho \otimes \boldsymbol{n})\right)$$
$$+ \frac{\gamma}{\epsilon}\nabla_\pi \cdot \left(\left(\frac{\partial \rho}{\partial \nu}\right)^2 (\boldsymbol{I} - \boldsymbol{n} \otimes \boldsymbol{n})\right) + O(1). \tag{B10}$$

After a few manipulations, one finds

$$\int \nabla \cdot K \, dn$$

$$= \gamma \int_{-\infty}^{\infty} dv, \left(\frac{\partial}{\partial v} \left(\frac{\partial \rho}{\partial v} \nabla_\pi \rho \right) + \frac{\partial \rho}{\partial v} \boldsymbol{n} \cdot \nabla_\pi \frac{\partial \rho}{\partial v} \boldsymbol{n} + \nabla_\pi \left(\frac{\partial \rho}{\partial v} \right)^2 - \kappa \left(\frac{\partial \rho}{\partial v} \right)^2 \boldsymbol{n} \right)$$

$$= \nabla_\pi \int_{-\infty}^{\infty} dv \, \gamma \left(\frac{\partial \rho}{\partial v} \right)^2 - \boldsymbol{n}\kappa \int_{-\infty}^{\infty} dv \, \gamma \left(\frac{\partial \rho}{\partial v} \right)^2 = \nabla_\pi \sigma - \kappa \sigma \boldsymbol{n}, \qquad (B11)$$

that is,

$$\int \nabla \cdot K \, dn = \nabla_\pi \sigma - \kappa \sigma \boldsymbol{n}, \qquad (B12)$$

with $\kappa = \nabla_\pi \cdot \boldsymbol{n}$ the mean curvature of the sharp interface.

Concerning the integral of the modified pressure gradient

$$\nabla \hat{p} = \frac{1}{\epsilon} \boldsymbol{n} \frac{\partial \hat{p}}{\partial v} + \nabla_\pi \hat{p}, \qquad (B13)$$

one obtains

$$\int \nabla \hat{p} \, dn = \boldsymbol{n} \int_{-\infty}^{\infty} \frac{\partial \hat{p}}{\partial v} \, dv + \epsilon \nabla_\pi \int_{-\infty}^{\infty} \hat{p} \, dv = \boldsymbol{n}[\hat{p}]_{-\infty}^{\infty} + \epsilon \nabla_\pi \int_{-\infty}^{\infty} \hat{p} \, dv. \qquad (B14)$$

Writing $\hat{p}$ in terms of derivatives with respect to *n*, as appropriate for the external solution, we find

$$[\hat{p}]_{-\infty}^{\infty} = [p_0]_{-\infty}^{\infty} + \epsilon \left[\frac{\gamma}{2} \left(\left(\frac{\partial \rho}{\partial n} \right)^2 + |\nabla_\pi \rho|^2 \right) - \gamma \rho \left(\frac{\partial^2 \rho}{\partial n^2} + \frac{\partial \rho}{\partial n} \nabla_\pi \cdot \boldsymbol{n} + \nabla_\pi^2 \rho \right) \right]_{-\infty}^{\infty}, \qquad (B15)$$

that is,

$$[\hat{p}]_{-\infty}^{\infty} = [p_0]_{-\infty}^{\infty}. \qquad (B16)$$

Concerning the surface gradient, to leading order,

$$\epsilon \nabla_\pi \int_{-\infty}^{\infty} dv \left(p_0 + \frac{\gamma}{2\epsilon} \left(\frac{\partial \rho}{\partial v} \right)^2 - \gamma \rho \frac{1}{\epsilon} \frac{\partial^2 \rho}{\partial v^2} \right). \qquad (B17)$$

Assuming local thermodynamic equilibrium across the interface, from the uniformity of the (generalised) chemical potential (Magaletti *et al.* 2016, 2021),

$$\mu_f = \mu_f^b - \lambda \nabla^2 \rho = \mu_{f\,eq}^b, \qquad (B18)$$

using the thin layer approximation $\nabla^2 \rho = 1/\epsilon^2 \partial^2 \rho / \partial v^2$, it follows

$$\frac{\lambda}{\epsilon} \frac{\partial^2 \rho}{\partial v^2} = \epsilon(\mu_f^b - \mu_{f\,eq}^b). \qquad (B19)$$

After multiplying by $1/\epsilon \, \partial \rho / \partial v$,

$$\frac{\lambda}{\epsilon^2} \frac{\partial \rho}{\partial v} \frac{\partial^2 \rho}{\partial v^2} = (\mu_f^b - \mu_{f\,eq}^b) \frac{\partial \rho}{\partial v}, \qquad (B20)$$

and realising that the left-hand side is $\lambda/(2\epsilon^2)\partial/\partial v((\partial\rho/\partial v)^2)$, rearranging the right-hand side as

$$(\mu_f^b - \mu_{f\,eq}^b)\frac{\partial\rho}{\partial v} = \frac{\partial}{\partial v}(f_f^b - \mu_{f\,eq}^b\rho) = \frac{\partial w_0}{\partial v}, \tag{B21}$$

where $w_0 = f_f^b - \mu_{f\,eq}^b\rho$, integration yields

$$\frac{\lambda}{2\epsilon^2}\left(\frac{\partial\rho}{\partial v}\right)^2 = w_0 - \bar{w}_0, \tag{B22}$$

where $\bar{w}_0$ is a suitable integration constant to be identified. Inserting (B19) and (B22) in (B17) leads to

$$\nabla_\pi \int_{-\infty}^{\infty} \mathrm{d}v \left(\epsilon p_0 + \frac{\gamma}{2}\left(\frac{\partial\rho}{\partial v}\right)^2 - \gamma\rho\frac{\partial^2\rho}{\partial v^2}\right)$$
$$= \epsilon\nabla_\pi \int_{-\infty}^{\infty} \mathrm{d}v\,(p_0 + (w_0 - \bar{w}_0) - \rho(\mu_f^b - \mu_{f\,eq}^b)) = O(\epsilon). \tag{B23}$$

Combining together the partial results, one finally obtains

$$\int \nabla\hat{p}\,\mathrm{d}n = [p_0]_{-\infty}^{\infty}\boldsymbol{n}. \tag{B24}$$

In conclusion, in the sharp interface limit,

$$\int \nabla\cdot\boldsymbol{T}_{rev}\,\mathrm{d}n = -[p_0]_{-\infty}^{\infty}\boldsymbol{n} + \nabla_\pi\sigma - \kappa\sigma\boldsymbol{n}. \tag{B25}$$

Thus, the interfacial layer, as seen by the external solution, appears as the locus of a concentrated force, leading to the well-known sharp interface form of the momentum conservation equation

$$\frac{\partial\rho\boldsymbol{u}}{\partial t} + \nabla\cdot(\rho\boldsymbol{u}\otimes\boldsymbol{u}) = \nabla\cdot\boldsymbol{T}_{visc} - \nabla p_0 + \nabla_\pi\sigma\delta(n) - \kappa\delta(n)\sigma\boldsymbol{n}. \tag{B26}$$

It is worth stressing that this result was reported in a slightly different derivation in Anderson *et al.* (1998). From the above equation, neglecting the Marangoni term $\nabla_\pi\sigma$, the evolution of vorticity is found to be described by the equation (Magnaudet & Mercier 2020)

$$\frac{\mathrm{D}}{\mathrm{D}t}\left(\frac{\boldsymbol{\zeta}}{\rho}\right) = \left(\frac{\boldsymbol{\zeta}}{\rho}\cdot\nabla\right)\boldsymbol{u} + \frac{1}{\rho^3}\nabla p_0\times\nabla\rho - \frac{1}{\rho}\nabla\left(\frac{\sigma\kappa}{\rho}\right)$$
$$\times\,\delta(n)\boldsymbol{n} + \frac{1}{\rho}\nabla\times\left(\frac{1}{\rho}\nabla\cdot\boldsymbol{\Sigma}\right). \tag{B27}$$

It should be stressed, however, that some of the terms appearing in the vorticity equation above cancel out exactly when obtaining the vorticity equation in the diffuse interface context. The reason is that the effect of capillarity can be expressed in terms of the gradient of the (generalised) chemical potential, $\nabla\cdot\boldsymbol{T}_{rev} = -\rho\nabla\mu_f - s_f\nabla\theta\nabla$, as shown in § 3.1, an aspect discussed also in a recent paper by Chen, Wang & Liu (2024).

REFERENCES

ABBONDANZA, D., GALLO, M. & CASCIOLA, C.M. 2023*a* Cavitation over solid surfaces: microbubble collapse, shock waves, and elastic response. *Meccanica* **58** (6), 1109–1119.

ABBONDANZA, D., GALLO, M. & CASCIOLA, C.M. 2023*b* Diffuse interface modeling of laser-induced nano-/micro-cavitation bubbles. *Phys. Fluids* **35** (2), 022113.

ADHIKARI, U., GOLIAEI, A. & BERKOWITZ, M.L. 2016 Nanobubbles, cavitation, shock waves and traumatic brain injury. *Phys. Chem. Chem. Phys.* **18** (48), 32638–32652.

AINSWORTH, M. & ODEN, J.T. 2011 *A Posteriori Error Estimation in Finite Element Analysis*. Pure and Applied Mathematics: a Wiley Series of Texts, Monographs and Tracts, vol. 37. John Wiley & Sons.

ANDERSON, D.M., MCFADDEN, G.B. & WHEELER, A.A. 1998 Diffuse-interface methods in fluid mechanics. *Annu. Rev. Fluid Mech.* **30** (1), 139–165.

ANDREWS, E.D., RIVAS, D.F. & PETERS, I.R. 2023 Bubble collapse near porous plates. *J. Fluid Mech.* **962**, A11.

ANTMAN, S.S. 2005 Problems in nonlinear elasticity. In *Nonlinear Problems of Elasticity*, pp. 513–584. Springer.

ANTMAN, S.S. & SZYMCZAK, W.G. 1989 Nonlinear elastoplastic waves. *Contemp. Maths* **100**, 27–54.

ARNDT, D., *et al.* 2023 The deal.II library, version 9.5. *J. Numer. Maths* **31** (3), 231–246.

BARNEY, C.W., *et al.* 2020 Cavitation in soft matter. *Proc. Natl Acad. Sci.* **117** (17), 9157–9165.

BENILOV, E.S. 2020 Dependence of the surface tension and contact angle on the temperature, as described by the diffuse-interface model. *Phys. Rev.* E **101** (4), 042803.

BENILOV, E.S. 2023 The multicomponent diffuse-interface model and its application to water/air interfaces. *J. Fluid Mech.* **954**, A41.

BOKMAN, G.T., BIASIORI-POULANGES, L., MEYER, D.W. & SUPPONEN, O. 2023 Scaling laws for bubble collapse driven by an impulsive shock wave. *J. Fluid Mech.* **967**, A33.

BOTTACCHIARI, M., GALLO, M., BUSSOLETTI, M. & CASCIOLA, C.M. 2022 Activation energy and force fields during topological transitions of fluid lipid vesicles. *Commun. Phys.* **5** (1), 283.

BREKHOVSKIKH, L.M. & GODIN, O.A. 2012 *Acoustics of Layered Media I: Plane and Quasi-plane Waves*, vol. 5. Springer Science & Business Media.

BREMS, S., HAUPTMANN, M., CAMEROTTO, E., PACCO, A., KIM, T.-G., XU, X., WOSTYN, K., MERTENS, P. & DE GENDT, S. 2013 Nanoparticle removal with megasonics: a review. *ECS J. Solid State Sci. Technol.* **3** (1), N3010.

BRENNEN, C.E. 2014 *Cavitation and Bubble Dynamics*. Cambridge University Press.

BRENNEN, C.E. 2015 Cavitation in medicine. *Interface Focus* **5** (5), 20150022.

BRENNER, M.P., HILGENFELDT, S. & LOHSE, D. 2002 Single-bubble sonoluminescence. *Rev. Mod. Phys.* **74** (2), 425.

BRUJAN, E.A., KEEN, G.S., VOGEL, A. & BLAKE, J.R. 2002 The final stage of the collapse of a cavitation bubble close to a rigid boundary. *Phys. Fluids* **14** (1), 85–92.

BRUJAN, E.-A., NAHEN, K., SCHMIDT, P. & VOGEL, A. 2001 Dynamics of laser-induced cavitation bubbles. *J. Fluid Mech.* **433**, 283–314.

CAO, S., WANG, G., COUTIER-DELGOSHA, O. & WANG, K. 2021 Shock-induced bubble collapse near solid materials: effect of acoustic impedance. *J. Fluid Mech.* **907**, A17.

CHAHINE, G.L. & HSIAO, C.-T. 2015 Modelling cavitation erosion using fluid–material interaction simulations. *Interface Focus* **5** (5), 20150016.

CHEN, T., WANG, C. & LIU, T. 2024 Interfacial vorticity dynamics for Navier–Stokes–Korteweg system: general theory and application to two-dimensional near-wall cavitation bubble. *Intl J. Multiphase Flow* **172**, 104705.

COUSSIOS, C.C. & ROY, R.A. 2008 Applications of acoustics and cavitation to noninvasive therapy and drug delivery. *Annu. Rev. Fluid Mech.* **40**, 395–420.

DEBENEDETTI, P.G. 2021 *Metastable Liquids*. Princeton University Press.

DROZDOV, A.D. & DE CLAVILLE CHRISTIANSEN, J. 2018 Time-dependent response of hydrogels under multiaxial deformation accompanied by swelling. *Acta Mech.* **229** (12), 5067–5092.

DULAR, M., DELGOSHA, O.C. & PETKOVŠEK, M. 2013 Observations of cavitation erosion pit formation. *Ultrason. Sonochem.* **20** (4), 1113–1120.

DULAR, M., POŽAR, T., ZEVNIK, J. & PETKOVŠEK, R. 2019 High speed observation of damage created by a collapse of a single cavitation bubble. *Wear* **418**, 13–23.

GAKENHEIMER, D.C. 1971 Response of an elastic half space to expanding surface loads. *J. Appl. Mech.* **38** (1), 99–110.

GAKENHEIMER, D.C. & MIKLOWITZ, J. 1969 Transient excitation of an elastic half space by a point load traveling on the surface. *J. Appl. Mech.* **36** (3), 505–515.

GALLO, M., MAGALETTI, F. & CASCIOLA, C.M. 2018 Thermally activated vapor bubble nucleation: the Landau–Lifshitz–van der Waals approach. *Phys. Rev. Fluids* **3** (5), 053604.

GALLO, M., MAGALETTI, F. & CASCIOLA, C.M. 2021 Heterogeneous bubble nucleation dynamics. *J. Fluid Mech.* **906**, A20.

GALLO, M., MAGALETTI, F., COCCO, D. & CASCIOLA, C.M. 2020 Nucleation and growth dynamics of vapour bubbles. *J. Fluid Mech.* **883**, A14.

GALLO, M., MAGALETTI, F., GEORGOULAS, A., MARENGO, M., DE CONINCK, J. & CASCIOLA, C.M. 2023 A nanoscale view of the origin of boiling and its dynamics. *Nat. Commun.* **14** (1), 6428.

GONZALEZ-AVILA, S.R., DENNER, F. & OHL, C.-D. 2021 The acoustic pressure generated by the cavitation bubble expansion and collapse near a rigid wall. *Phys. Fluids* **33** (3), 032118.

GRAFF, K.F. 2012 *Wave Motion in Elastic Solids*. Courier Corporation.

GURTIN, M.E. 1982 *An Introduction to Continuum Mechanics*. Academic Press.

GURTIN, M.E., FRIED, E. & ANAND, L. 2010 *The Mechanics and Thermodynamics of Continua*. Cambridge University Press.

GUTIÉRREZ-HERNÁNDEZ, U.J., REESE, H., OHL, C.-D. & QUINTO-SU, P.A. 2023 Controlled inertial nano-cavitation above 100 MHz. *J. Fluid Mech.* **972**, A16.

GUVENDIREN, M. & BURDICK, J.A. 2012 Stiffening hydrogels to probe short-and long-term cellular responses to dynamic mechanics. *Nat. Commun.* **3** (1), 1–9.

HENDERSON, L.F. 1989 On the refraction of shock waves. *J. Fluid Mech.* **198**, 365–386.

HU, T., WANG, H. & GOMEZ, H. 2023 Direct van der Waals simulation (DVS) of phase-transforming fluids. *Sci. Adv.* **9** (11), eadg3007.

HUGHES, T.J.R. 2012 *The Finite Element Method: Linear Static and Dynamic Finite Element Analysis*. Courier Corporation.

JAMET, D. 2001 Diffuse interface models in fluid mechanics. *GdR CNRS Documentation*. Available at: http://pmc.polytechnique.fr/mp/GDR/docu/Jamet.pdf

JAMET, D., LEBAIGUE, O., COUTRIS, N. & DELHAYE, J.M. 2001 The second gradient method for the direct numerical simulation of liquid–vapor flows with phase change. *J. Comput. Phys.* **169** (2), 624–651.

JOHNSEN, E. & COLONIUS, T. 2009 Numerical simulations of non-spherical bubble collapse. *J. Fluid Mech.* **629**, 231–262.

KELLY, D.W., DE SR GAGO, J.P., ZIENKIEWICZ, O.C. & BABUSKA, I. 1983 A posteriori error analysis and adaptive processes in the finite element method. Part I. Error analysis. *Intl J. Numer. Meth. Engng* **19** (11), 1593–1619.

KODAMA, T. & TAKAYAMA, K. 1998 Dynamic behavior of bubbles during extracorporeal shock-wave lithotripsy. *Ultrasound Med. Biol.* **24** (5), 723–738.

LAUTERBORN, W. & BOLLE, H. 1975 Experimental investigations of cavitation-bubble collapse in the neighbourhood of a solid boundary. *J. Fluid Mech.* **72** (2), 391–399.

LECHNER, C., LAUTERBORN, W., KOCH, M. & METTIN, R. 2020 Jet formation from bubbles near a solid boundary in a compressible liquid: numerical study of distance dependence. *Phys. Rev. Fluids* **5** (9), 093604.

LIU, J., AMBERG, G. & DO-QUANG, M. 2016 Diffuse interface method for a compressible binary fluid. *Phys. Rev.* E **93** (1), 013121.

LIU, Z., TOH, W. & NG, T.Y. 2015 Advances in mechanics of soft materials: a review of large deformation behavior of hydrogels. *Intl J. Appl. Mech.* **7** (5), 1530001.

LOVE, A.E.H. 1911 *Some Problems of Geodynamics: Being an Essay to Which the Adams Prize in the University of Cambridge was Adjudged in 1911*, vol. 911. University Press.

LUBLINER, J. 1972 On the thermodynamic foundations of non-linear solid mechanics. *Intl J. Non-Linear Mech.* **7** (3), 237–254.

LUBLINER, J. 2008 *Plasticity Theory*. Courier Corporation.

MAGALETTI, F., GALLO, M. & CASCIOLA, C.M. 2021 Water cavitation from ambient to high temperatures. *Sci. Rep.* **11** (1), 1–10.

MAGALETTI, F., GALLO, M., MARINO, L. & CASCIOLA, C.M. 2016 Shock-induced collapse of a vapor nanobubble near solid boundaries. *Intl J. Multiphase Flow* **84**, 34–45.

MAGALETTI, F., MARINO, L. & CASCIOLA, C.M. 2015 Shock wave formation in the collapse of a vapor nanobubble. *Phys. Rev. Lett.* **114** (6), 064501.

MAGALETTI, F, PICANO, F., CHINAPPI, M., MARINO, L. & CASCIOLA, C.M. 2013 The sharp-interface limit of the Cahn–Hilliard/Navier–Stokes model for binary fluids. *J. Fluid Mech.* **714**, 95–126.

MAGNAUDET, J. & MERCIER, M.J. 2020 Particles, drops, and bubbles moving across sharp interfaces and stratified layers. *Annu. Rev. Fluid Mech.* **52** (1), 61–91.

MANCIA, L., VLAISAVLJEVICH, E., YOUSEFI, N., RODRIGUEZ, M., ZIEMLEWICZ, T.J., LEE, F.T., HENANN, D., FRANCK, C., XU, Z. & JOHNSEN, E. 2019 Modeling tissue-selective cavitation damage. *Phys. Med. Biol.* **64** (22), 225001.

MIKLOWITZ, J. 2012 *The Theory of Elastic Waves and Waveguides*. Elsevier.

MILLER, D.L., PISLARU, S.V. & GREENLEAF, J.F. 2002 Sonoporation: mechanical DNA delivery by ultrasonic cavitation. *Somat. Cell Mol. Genet.* **27** (1), 115–134.

MISES, R. 1928 Mechanics of plastic shape change of crystals. *Z. Angew. Math. Mech.* **8**, 161–185.

MISES, R.V. 1913 Mechanik der festen Körper im plastisch-deformablen zustand. *Nachrichten von der Gesellschaft der Wissenschaften zu Göttingen, Mathematisch-Physikalische Klasse*, pp. 582–592.

MNICH, D., REUTER, F., DENNER, F. & OHL, C.-D. 2024 Single cavitation bubble dynamics in a stagnation flow. *J. Fluid Mech.* **979**, A18.

MUKHERJEE, S. & GOMEZ, H. 2022 Effect of dissolved gas on the tensile strength of water. *Phys. Fluids* **34** (12), 126112.

NEWMARK, N.M. 1959 A method of computation for structural dynamics. *J. Engng Mech. Div.* **85** (3), 67–94.

NOBLIN, X., ROJAS, N.O., WESTBROOK, J., LLORENS, C., ARGENTINA, M. & DUMAIS, J. 2012 The fern sporangium: a unique catapult. *Science* **335** (6074), 1322–1322.

OCCHICONE, A., SINIBALDI, G., DANZ, N., CASCIOLA, C.M. & MICHELOTTI, F. 2019 Cavitation bubble wall pressure measurement by an electromagnetic surface wave enhanced pump-probe configuration. *Appl. Phys. Lett.* **114** (13), 134101.

OHL, C.D. & IKINK, R. 2003 Shock-wave-induced jetting of micron-size bubbles. *Phys. Rev. Lett.* **90** (21), 214502.

PERUZZI, G., SINIBALDI, G., SILVANI, G., RUOCCO, G. & CASCIOLA, C.M. 2018 Perspectives on cavitation enhanced endothelial layer permeability. *Colloids Surf.* B **168**, 83–93.

PFEIFFER, P., SHAHROOZ, M., TORTORA, M., CASCIOLA, C.M., HOLMAN, R., SALOMIR, R., MELONI, S. & OHL, C.-D. 2022 Heterogeneous cavitation from atomically smooth liquid-liquid interfaces. *Nat. Phys.* **18** (12), 1431–1435.

PHILIPP, A. & LAUTERBORN, W. 1998 Cavitation erosion by single laser-produced bubbles. *J. Fluid Mech.* **361**, 75–116.

PLESSET, M.S. & CHAPMAN, R.B. 1971 Collapse of an initially spherical vapour cavity in the neighbourhood of a solid boundary. *J. Fluid Mech.* **47** (2), 283–290.

PONOMARENKO, A., VINCENT, O., PIETRIGA, A., COCHARD, H., BADEL, É. & MARMOTTANT, P. 2014 Ultrasonic emissions reveal individual cavitation bubbles in water-stressed wood. *J. R. Soc. Interface* **11** (99), 20140480.

RANJAN, D., OAKLEY, J. & BONAZZA, R. 2011 Shock-bubble interactions. *Annu. Rev. Fluid Mech.* **43**, 117–140.

RASTHOFER, U., WERMELINGER, F., KARNAKOV, P., ŠUKYS, J. & KOUMOUTSAKOS, P. 2019 Computational study of the collapse of a cloud with 12 500 gas bubbles in a liquid. *Phys. Rev. Fluids* **4** (6), 063602.

RATTRAY, M. 1951 Perturbation effects in cavitation bubble dynamics. PhD thesis, California Institute of Technology.

RAYLEIGH, L. 1885 On waves propagated along the plane surface of an elastic solid. *Proc. Lond. Math. Soc.* **1** (1), 4–11.

REESE, H., OHL, S.-W. & OHL, C.-D. 2023 Cavitation bubble induced wall shear stress on an elastic boundary. *Phys. Fluids* **35** (7), 076122.

REUTER, F., DEITER, C. & OHL, C.-D. 2022 Cavitation erosion by shockwave self-focusing of a single bubble. *Ultrason. Sonochem.* **90**, 106131.

ROBINSON, J.P., MACEDO, R.G., VERHAAGEN, B., VERSLUIS, M., COOPER, P.R., VAN DER SLUIS, L.W.M. & WALMSLEY, A.D. 2018 Cleaning lateral morphological features of the root canal: the role of streaming and cavitation. *Intl Endod. J.* **51**, e55–e64.

ROBINSON, P.B., BLAKE, J.R., KODAMA, T., SHIMA, A. & TOMITA, Y. 2001 Interaction of cavitation bubbles with a free surface. *J. Appl. Phys.* **89** (12), 8225–8237.

SAADE, Y., LOHSE, D. & FUSTER, D. 2023 A multigrid solver for the coupled pressure-temperature equations in an all-Mach solver with VOF. *J. Comput. Phys.* **476**, 111865.

SAINI, M., TANNE, E., ARRIGONI, M., ZALESKI, S. & FUSTER, D. 2022 On the dynamics of a collapsing bubble in contact with a rigid wall. *J. Fluid Mech.* **948**, A45.

SCOGNAMIGLIO, C., MAGALETTI, F., IZMAYLOV, Y., GALLO, M., CASCIOLA, C.M. & NOBLIN, X. 2018 The detailed acoustic signature of a micro-confined cavitation bubble. *Soft Matt.* **14** (39), 7987–7995.

SILVANI, G., SCOGNAMIGLIO, C., CAPRINI, D., MARINO, L., CHINAPPI, M., SINIBALDI, G., PERUZZI, G., KIANI, M.F. & CASCIOLA, C.M. 2019 Reversible cavitation-induced junctional opening in an artificial endothelial layer. *Small* **15** (51), 1905375.

SIMO, J.C. & HUGHES, T.J.R. 2006 *Computational Inelasticity*, vol. 7. Springer Science & Business Media.

SIMO, J.C. & TAYLOR, R.L. 1985 Consistent tangent operators for rate-independent elastoplasticity. *Comput. Meth. Appl. Mech. Engng* **48** (1), 101–118.

SINIBALDI, G., OCCHICONE, A., ALVES PEREIRA, F., CAPRINI, D., MARINO, L., MICHELOTTI, F. & CASCIOLA, C.M. 2019 Laser induced cavitation: plasma generation and breakdown shockwave. *Phys. Fluids* **31** (10), 103302.

STRIPLING, L.B. & ACOSTA, A.J. 1962 Cavitation in turbopumps. Part 1. *J. Basic Eng.* **84** (3), 326–338.

TAYLOR, G.I. 1947 A connexion between the criterion of yield and the strain ratio relationship in plastic solids. *Proc. R. Soc. Lond.* A *Math. Phys. Sci.* **191** (1027), 441–446.

TERRINGTON, S.J., HOURIGAN, K. & THOMPSON, M.C. 2020 The generation and conservation of vorticity: deforming interfaces and boundaries in two-dimensional flows. *J. Fluid Mech.* **890**, A5.

TERRINGTON, S.J., HOURIGAN, K. & THOMPSON, M.C. 2021 The generation and diffusion of vorticity in three-dimensional flows: Lyman's flux. *J. Fluid Mech.* **915**, A106.

TERRINGTON, S.J., HOURIGAN, K. & THOMPSON, M.C. 2022 Vorticity generation and conservation on generalised interfaces in three-dimensional flows. *J. Fluid Mech.* **936**, A44.

THO, P., MANASSEH, R. & OOI, A. 2007 Cavitation microstreaming patterns in single and multiple bubble systems. *J. Fluid Mech.* **576**, 191–233.

TOMITA, Y. & SHIMA, A. 1986 Mechanisms of impulsive pressure generation and damage pit formation by bubble collapse. *J. Fluid Mech.* **169**, 535–564.

VINCENT, O., MARMOTTANT, P., QUINTO-SU, P.A. & OHL, C.-D. 2012 Birth and growth of cavitation bubbles within water under tension confined in a simple synthetic tree. *Phys. Rev. Lett.* **108** (18), 184502.

VOGEL, A., HENTSCHEL, W., HOLZFUSS, J. & LAUTERBORN, W. 1986 Cavitation bubble dynamics and acoustic transient generation in ocular surgery with pulsed neodymium: YAG lasers. *Ophthalmology* **93** (10), 1259–1269.

VON KÁRMÁN, T. & DUWEZ, P. 1950 The propagation of plastic deformation in solids. *J. Appl. Phys.* **21** (10), 987–994.

VON SCHMIDT, O. 1938 Über knallwellenausbreitung in flüssigkeiten und festen körpern. *Z. Tech. Phys.* **19**, 554–561.

VAN DER WAALS, J.D. 1893 Thermodynamische theorie der capillariteit in de onderstelling van continue dichtheidsverandering. *Verh. K. Akad. Wet. Amsterdam* **1**.

VAN DER WAALS, J.D. 1979 The thermodynamic theory of capillarity under the hypothesis of a continuous variation of density (English translation J.S. Rowlinson). *J. Stat. Phys.* **20** (2), 200–244.

WU, H., ZHENG, H., LI, Y., OHL, C.-D., YU, H. & LI, D. 2021 Effects of surface tension on the dynamics of a single micro bubble near a rigid wall in an ultrasonic field. *Ultrason. Sonochem.* **78**, 105735.

XU, H., ZEIGER, B.W. & SUSLICK, K.S. 2013 Sonochemical synthesis of nanomaterials. *Chem. Soc. Rev.* **42** (7), 2555–2567.

ZENG, Q., AN, H. & OHL, C.-D. 2022 Wall shear stress from jetting cavitation bubbles: influence of the stand-off distance and liquid viscosity. *J. Fluid Mech.* **932**, A14.

ZENG, Q., GONZALEZ-AVILA, S.R., DIJKINK, R., KOUKOUVINIS, P., GAVAISES, M. & OHL, C.-D. 2018 Wall shear stress from jetting cavitation bubbles. *J. Fluid Mech.* **846**, 341–355.

ZHANG, S., DUNCAN, J.H. & CHAHINE, G.L. 1993 The final stage of the collapse of a cavitation bubble near a rigid wall. *J. Fluid Mech.* **257**, 147–181.

ZHAO, N., MENTRELLI, A., RUGGERI, T. & SUGIYAMA, M. 2011 Admissible shock waves and shock-induced phase transitions in a van der Waals fluid. *Phys. Fluids* **23** (8), 086101.

ZHONG, P. 2013 *Shock wave lithotripsy. Bubble Dynamics and Shock Waves*, 291–338. Springer.